

Bachelor's Thesis (Academic Year 2025)

# Scalable Optical Switching Architectures for Quantum Photonic Networks

Keio University  
Faculty of environment and information studies

Marii Koyama

January 2026

# Bachelor's Thesis Abstract Academic Year 2025

## Scalable Optical Switching Architectures for Quantum Photonic Networks

### Summary

Scalable quantum networks require distributing high quality entanglement between many remote quantum nodes. In leading architectures, this is achieved by routing photonic signals to a shared pool of Bell state measurement(BSM) modules, rather than dedicating one BSM to every communicating pair. As the network size grows, the switching fabric becomes a dominant contributor to cost and loss. Therefore, an architecture that scales to large port counts while minimizing the number of optical switching elements is desirable.

This thesis studies modular  $M \times M$  switching fabrics for constructing an  $N \times N$  photonic switch suitable for quantum networking. First, I analyze the required number of  $M \times M$  switches and present proof for a minimal switch count, together with a constructive design that achieves this bound and the corresponding routing algorithms. Second, I design and simulate integrated photonic switch building blocks in Ansys Lumerical at a target wavelength of  $\lambda = 422$  nm using Ge-doped SiO<sub>2</sub> waveguides. Using eigenmode and propagation simulations, I optimize structures and report insertion loss, extinction ratio, and routing behavior for  $2 \times 2$  devices. Finally, I discuss how these building blocks compose into larger fabrics and summarize design trade-offs between scalability, loss, and control complexity.

### Keywords

Quantum networks, Photonic switching, Non-blocking switching networks, Integrated photonics, Entanglement distribution

Faculty of environment and information studies  
Keio University

Marii Koyama

## 卒業論文 2025 年度（平成 7 年度）

# Scalable Optical Switching Architectures for Quantum Photonic Networks

## 論文要旨

大規模な量子ネットワークを実現するためには、多数の量子ノード間で高品質な量子もつれを効率よく分配する必要がある。現在提案されているアーキテクチャでは、すべてのノード間に測定機を用意するのではなく、複数のノード間でベル状態測定器を共有し、光子のシグナルを必要に応じて動的にルーティングする方式がある。ネットワーク規模の拡大によって、シグナルをルーティングする光スイッチファブリックがコスト及び光損失の要因になる。そのため、大規模ポートにスケーリング可能であり、かつ、必要な光スイッチ素子数を最小化するアーキテクチャが望ましい。

本論文では、 $N \times N$  の光スイッチを  $M \times M$  のモジュールスイッチで構成するスイッチファブリックについて取り組む。まず、必要となる  $M \times M$  スイッチ数を解析し、最小スイッチ数を導出するとともに、スイッチの構成法及び対応するルーティングアルゴリズムを示す。次に、 $\lambda = 422\text{nm}$  を目標波長とした、Ge ドープ  $\text{SiO}_2$  導波路を用いた集積フォトニクス素子を Ansys Lumerical により設計・シミュレーションする。このシミュレーションにより各コンポーネントの最適化を行い、 $2 \times 2$  および  $3 \times 3$  スイッチの損失及びルーティング特性を評価する。最後に、これらのデバイスを大規模化する際の構成について議論し、スケーラビリティ、損失、制御の複雑性について考察する。

## キーワード

量子ネットワーク、フォトニックスイッティング、ノンブロッキングスイッチネットワーク、集積フォトニクス、量子もつれ分配

慶應義塾大学 環境情報学部

Marii Koyama

# Contents

<b>1</b>	<b>Introduction</b>	<b>1</b>
1.1	Overview . . . . .	1
1.2	Problem Definition . . . . .	1
1.3	Research contribution . . . . .	2
1.4	Thesis Structure . . . . .	3
<b>2</b>	<b>Basics of Quantum Information</b>	<b>4</b>
2.1	Qubits and Quantum States . . . . .	4
2.1.1	Matrix representation of states . . . . .	5
2.1.2	Quantum gates . . . . .	6
2.1.3	Measurement and Basis . . . . .	7
2.2	Entanglement and Bell basis . . . . .	8
2.3	Quantum Communication . . . . .	8
2.3.1	Quantum teleportation . . . . .	8
2.3.2	Entanglement distribution and quantum repeaters . . . . .	9
2.3.3	Applications . . . . .	10
2.4	Motivation for Integrated Photonics in Quantum Networks . . . . .	11
2.5	Fundamentals of optics for Quantum Chips . . . . .	11
2.5.1	Quantum description of light . . . . .	11
2.5.2	Optical Waveguides . . . . .	13
2.5.3	Directional Couplers . . . . .	13
2.5.4	Phase-shifting Components . . . . .	13
2.5.5	Mach-Zehnder Interferometer (MZI) . . . . .	14
2.6	Noise in Quantum systems . . . . .	15
2.6.1	Photon loss and insertion loss . . . . .	15
2.6.2	Phase noise and stability . . . . .	15
2.6.3	Mode mismatch and distinguishability . . . . .	15
2.6.4	Impact on entanglement distribution . . . . .	15
<b>3</b>	<b>Structure of Quantum Interconnects</b>	<b>17</b>
3.1	System model of the Quantum Network . . . . .	17
3.1.1	Network component and interfaces . . . . .	17
3.1.2	Operation flow . . . . .	19
3.1.3	Timing and synchronization . . . . .	19
3.1.4	Representative interconnect topologies . . . . .	20
3.1.5	Architectural implications for switch requirements . . . . .	22
<b>4</b>	<b>Optical switching design for Quantum Interconnects</b>	<b>25</b>

4.1	Overview of Optical switching . . . . .	25
4.2	Switching Notations and Performance Metrics . . . . .	25
4.3	Existing Switching Architecture . . . . .	26
4.4	Minimal switch count for planar pair-to-BSA routing . . . . .	26
4.4.1	Problem setting and worst-case pairing . . . . .	26
4.4.2	Parity and termination at two channels . . . . .	28
4.4.3	Layer-wise reduction argument . . . . .	28
4.4.4	Result and consistency check for $M = 2$ . . . . .	29
4.5	Design and routing . . . . .	29
4.5.1	Routing principle . . . . .	30
4.5.2	Recursive designs . . . . .	31
4.5.3	Hybrid layout . . . . .	36
4.6	Generalized Interconnect Fabrics . . . . .	40
<b>5</b>	<b>Chip Specification</b>	<b>42</b>
5.1	Purpose and scope . . . . .	42
5.2	Platform Choices . . . . .	42
5.2.1	Wavelength . . . . .	43
5.2.2	Waveguide Platform . . . . .	43
5.2.3	Switching Mechanism . . . . .	43
5.3	Design Constraints . . . . .	44
5.3.1	Fabrication and Geometry constraints . . . . .	44
5.3.2	Optical functional constraints . . . . .	44
5.4	Design assumptions . . . . .	45
<b>6</b>	<b>Simulation Methodology</b>	<b>47</b>
6.1	Overview of Simulation Workflow . . . . .	47
6.2	Numerical Solvers . . . . .	47
6.2.1	Finite Difference Eigenmode(FDE) . . . . .	48
6.2.2	Bidirectional Eigenmode Expansion(EME) . . . . .	48
6.2.3	Heat Transport(HEAT) . . . . .	48
6.3	Material Definition . . . . .	48
6.3.1	Waveguide Dimension Design . . . . .	48
6.3.2	Directional Coupler Design . . . . .	49
6.3.3	Non-Coupling Region . . . . .	51
6.3.4	S-Bend Design . . . . .	52
6.3.5	Mach Zehnder Interferometer(MZI) . . . . .	52
6.3.6	Thermo-Optic Heater Design . . . . .	55
6.4	Summary . . . . .	57

<b>7 Evaluation and Discussion</b>	<b>58</b>
7.1 Scalability and Resource Analysis . . . . .	58
7.2 Expected Physical Performance . . . . .	59
7.2.1 Preliminary switching behavior . . . . .	59
7.2.2 Vertical cascading and loss accumulation . . . . .	60
7.2.3 Scope and limitations of the current simulations . . . . .	60
7.2.4 Interpretation and outlook . . . . .	61
7.3 Comparison of Switch Element Sizes . . . . .	62
7.4 Literature-Based Loss Analysis and Discussion . . . . .	63
<b>8 Conclusion</b>	<b>65</b>
8.1 Future Work . . . . .	65
8.1.1 Extension to Multicomputer Network Architectures . . . . .	66
8.1.2 Device-Level Optimization and Fabrication-Oriented Design . . . . .	66
8.1.3 Outlook . . . . .	66
<b>Acknowledgment</b>	<b>67</b>
<b>Bibliography</b>	<b>68</b>

## List of Figures

2.1	Bloch sphere representation . . . . .	4
2.2	Image of figure for quantum teleportation . . . . .	9
3.1	Shared-BSA-pool and Shared-EPPS-pool interconnect . . . . .	22
3.2	Modular quantum computer interconnect motifs that rely on optical switching	23
3.3	Heterogeneous interconnect . . . . .	24
4.1	Existing switching architectures for quantum networks. . . . .	27
4.2	Overview of the optical switching architecture. . . . .	27
4.3	Two triangular $3 \times 3$ fabrics for $N = 12$ with different stage extraction capacities. . . . .	32
4.4	Recursive example for triangular $2 \times 2$ fabrics for $N = 10$ . . . . .	32
4.5	Two pizza slice $3 \times 3$ fabrics for $N = 12$ . . . . .	34
4.6	Recursive example for pizza slice $2 \times 2$ fabrics for $N = 10$ . . . . .	35
4.7	Two chevron $3 \times 3$ fabrics for $N = 12$ . . . . .	35
4.8	Recursive example for chevron $2 \times 2$ fabrics for $N = 10$ . . . . .	38
4.9	Hybrid-family construction examples for $M = 3$ . . . . .	39
4.10	Recursive example for brickwork $2 \times 2$ fabrics for $N = 10$ . . . . .	40
5.1	Operation principle of a Mach – Zehnder interferometer based $2 \times 2$ switch. .	43
6.1	Propagation loss versus waveguide dimensions for the first three supported modes. . . . .	50
6.2	Simulated coupling ratio and insertion loss of the directional coupler. . . . .	52
6.3	Simulation monitor for s-bend connecting coupling and non-coupling region.	53
6.4	Simulation monitor and S-matrix of the MZI in CROSS state. . . . .	55
6.5	Simulation monitor and S-matrix of the MZI in BAR state. . . . .	56
7.1	Comparison of switch count scaling for different architectures. . . . .	59
7.2	Accumulated insertion loss for vertically cascaded switching stages assuming a single-switch insertion loss of 0.8 dB. . . . .	61
7.3	Estimated chip-level loss proxy based on literature-reported switch losses. .	64

## List of Tables

3.1	Representative quantum interconnect architectures and the corresponding implications for optical switching fabrics. . . . .	24
5.1	Design constraints and simulation status of the $2 \times 2$ thermo-optic MZI switch. . . . .	46
7.1	Representative MMI-based optical switches with explicitly reported insertion loss in telecom wavelengths. . . . .	63

# Chapter 1

## Introduction

### 1.1 Overview

Quantum networks aim to distribute entanglement between remote quantum nodes to enable applications such as distributed quantum computing, quantum key distribution, and quantum sensing [43, 24, 41, 21, 16]. In many architectures, stationary qubits, as trapped ions, serve as quantum memories, while photons act as flying qubits that carry quantum information through optical channels to different quantum nodes[30, 39]. A practical network must be able to route photons from selected nodes to a Bell state measurement device, so a heralded entanglement between distant nodes can be generated and extended [7, 45, 8].

As the number of nodes in the network grows, it becomes costly and difficult to scale by dedicating separate Bell State Analyzers(BSAs) to every possible communicating pair. A more scalable approach is to share a limited pool of BSAs among nodes, and dynamically route photons to available BSA ports[19, 37]. In order to realize this, such an optical switching fabric will be required, that can connect arbitrary input photons to BSA inputs, while maintaining high interference visibility, and is able to scale to any port counts.

Integrated photonics is attracting attention as a platform for implementing such kinds of routing devices. Compared to bulk optics, photonic integrated circuits offer compactness, stability, and compatibility with scalable fabrication [31, 42, 17]. In this thesis I focus on the design problem across two levels:

**Network level switching design** - How to build a large fabric from modular blocks.

**Device level switch cell design** - How to realize a low loss elementary switch cell.

### 1.2 Problem Definition

I consider two coupled research questions: a network-level architecture question and a device-level component design question.

### i. Network level: Minimal switch scalable architecture

Let  $N$  denote the number of photonic input channels (network size), and let  $M$  denote the radix of the modular building block, as  $M \times M$  switch. I propose a switching architecture that is,

**Rearrangeably non-blocking:** Able to realize any required connection.

**Planar:** No waveguide overlaps in the design to realize fabrication.

**Scalable:** Extendable to any  $N$  by composing modular blocks.

**Switch efficient:** Minimizes the total number of  $M \times M$  switch elements required.

This leads to the following research question:

*What is the minimal number of  $M \times M$  switches required to construct an  $N \times N$  switching fabric capable of routing arbitrary input pairs to common BSA ports?*

### ii. Device level: Low loss $2 \times 2$ switch cell design at an ion compatible wavelength

Most of the mature optical switching components are designed for telecom wavelengths, while many ion-based quantum networking interfaces use visible or near-visible wavelengths. Therefore, to evaluate the feasibility of integrated switching in such settings, it is necessary to quantify device performance at an ion compatible wavelength[11].

Even if a network architecture is optimal in switch count, it is only useful if the underlying switch cell achieves sufficiently low insertion loss and sufficient switching contrast.

I therefore address the following device level research question:

*How can a low-loss, high contrast  $2 \times 2$  integrated photonic switch cell be designed and validated at  $\lambda = 422$  nm as a building block for scalable switching fabrics?*

## 1.3 Research contribution

The main contributions of this thesis are,

1. **Minimal switch count analysis and constructive architectures:** I analyze and propose switching architectures that minimize the number of modular  $M \times M$  elements required to realize an  $N \times N$  reconfigurable non-blocking fabric for BSA sharing.
2. **Structured multi-stage designs and routing viewpoints:** I discuss structured layouts that support systematic routing while remaining physically realizable and scalable.
3. **Simulation driven design workflow for an ion-compatible  $2 \times 2$  switch cell:** I establish a design and verification workflow in Ansys Lumerical to obtain a low-loss  $2 \times 2$  MZI switch at  $\lambda = 422$  nm in a silica-based platform.

## 1.4 Thesis Structure

The content of the thesis is organized as follows.

**Chapter 2 Basics of Quantum Information** introduces the quantum-information and photonics background needed for the later chapters, including qubits, entanglement, teleportation, repeater concepts, and the core integrated optics components used to implement photonic switching.

**Chapter 3 Structure of Quantum Interconnects** defines the system model of the quantum network assumed in this work, including the roles of quantum nodes, flying qubits, BSAs, switching fabrics, and timing constraints.

**Chapter 4 Optical Switching Design for Quantum Interconnects** develops the switching design for quantum networks, surveys relevant architectures, and presents minimal switch-count analysis with structured designs.

**Chapter 5 Chip Specification** specifies the target chip platform and constraints, including wavelength choice, material system, switching mechanism, and design metrics.

**Chapter 6 Simulation Methodology** details the simulation methodology and workflow in Ansys Lumerical used to design and validate the  $2 \times 2$  switch cell.

**Chapter 7 Evaluation** summarizes evaluation results and discusses remaining gaps and practical considerations.

**Chapter 8 Conclusion** concludes the thesis and outlines future work directions.

## Chapter 2

# Basics of Quantum Information

### 2.1 Qubits and Quantum States

In quantum information, information is carried in a fundamental unit known as *qubit*. As in the classical world, where bits can take two values 0 or 1, qubits have two basis states, denoted as  $|0\rangle$  and  $|1\rangle$  [29]. However, unlike classical bits, a qubit can also exist in a *superposition* of these basis states. Superposition can be imagined as a mix of states, where the output can vary depending on the basis you measure the qubit.

A qubit state can be denoted as:

$$|\psi\rangle = \alpha|0\rangle + \beta|1\rangle, \quad \text{where } \alpha, \beta \in \mathbb{C}, \quad |\alpha|^2 + |\beta|^2 = 1. \quad (2.1)$$

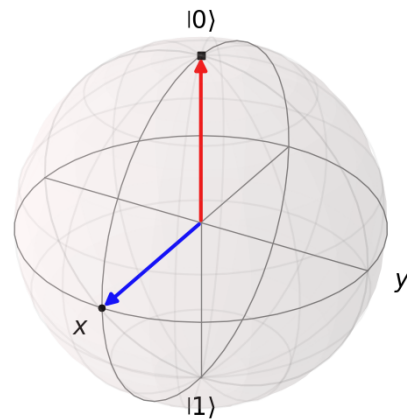


Figure 2.1: Bloch sphere representation

Red line represents state  $|\psi\rangle = |0\rangle$ , the blue line represents state  $|\psi\rangle = \frac{|0\rangle + |1\rangle}{\sqrt{2}}$ . Both states are on the surface of the sphere, thus are pure states.

One intuitive way to visualize the state of a qubit is by using the *Bloch sphere*, as shown in Fig. 2.1. The point illustrates the state of the qubit [29]. Pure states correspond to points on the surface of the sphere. For example, the state  $|0\rangle$  lies at the north pole of the sphere (the positive  $z$ -axis).

The state  $|+\rangle = \frac{1}{\sqrt{2}}(|0\rangle + |1\rangle)$  lies on the equator along the  $x$ -axis and represents an equal superposition of  $|0\rangle$  and  $|1\rangle$ . Therefore, when measuring this qubit, the results can be 0 or 1 with the same probability.

When the qubit is placed inside of the Bloch sphere, the state is called a *mixed state*. The more the qubit is placed near the center of the sphere, the knowledge we have about the state is limited. When the qubit is placed in the center of the sphere, the state is called *maximally mixed state*, and it means that the state of the qubit is completely unknown. While the Bloch sphere was an intuitive representation of a single qubit state, qubit states are practically used in mathematical representations. In quantum information processing, qubit states and operations are described using matrices and vectors.

### 2.1.1 Matrix representation of states

The computational basis states  $|0\rangle$  and  $|1\rangle$  are represented in vector form as

$$|0\rangle = \begin{pmatrix} 1 \\ 0 \end{pmatrix}, \quad |1\rangle = \begin{pmatrix} 0 \\ 1 \end{pmatrix}$$

From these basis vectors, we can derive any general qubit state as a linear combination,

$$|\psi\rangle = \alpha|0\rangle + \beta|1\rangle = \begin{pmatrix} \alpha \\ \beta \end{pmatrix}$$

where,  $\alpha, \beta \in \mathbb{C}$  and  $|\alpha|^2 + |\beta|^2 = 1$ . To compare quantum states and express measurement outcomes, we can calculate the *inner product* of two states. The inner product can measure the similarity of two states. For two states  $|\psi_1\rangle = \alpha|0\rangle + \beta|1\rangle$  and  $|\psi_2\rangle = \gamma|0\rangle + \delta|1\rangle$ , the inner product is denoted as,

$$\langle\psi_1|\psi_2\rangle = \begin{pmatrix} \alpha^* & \beta^* \end{pmatrix} \begin{pmatrix} \gamma \\ \delta \end{pmatrix} = \alpha^*\gamma + \beta^*\delta \quad (2.2)$$

$\langle\psi|$  is the Hermitian adjoint of the ket vector  $|\psi\rangle$ .

For example

$$\langle 0|0\rangle = 1, \quad \langle 1|1\rangle = 1, \quad \langle 0|1\rangle = 0$$

shows that the basis states are orthonormal, since there are no overlaps between  $|0\rangle$  and  $|1\rangle$  and the output is 0. The inner product allows us to calculate the probability amplitude of getting  $|\psi_1\rangle$  when measuring  $|\psi_2\rangle$ . This is derived by  $|\langle\psi_1|\psi_2\rangle|^2$ .

By changing the order of multiplication of the qubit states, we can obtain the *outer product*, which is used to obtain the *density matrix*. The outer product can describe both pure and mixed states. If we have a pure state  $|\psi\rangle = \alpha|0\rangle + \beta|1\rangle$ , we can express the pure state density matrix as,

$$\rho = |\psi\rangle\langle\psi| = \begin{pmatrix} \alpha \\ \beta \end{pmatrix} \begin{pmatrix} \alpha^* & \beta^* \end{pmatrix} = \begin{pmatrix} |\alpha|^2 & \alpha\beta^* \\ \alpha^*\beta & |\beta|^2 \end{pmatrix} \quad (2.3)$$

where, the matrix represents a *pure state*, because it is constructed from same state vectors. Another way to know whether the state is pure is by taking its trace, if the trace is 1, the state is pure. In this case,  $\text{Tr}\rho^2 = 1$ .

A *mixed state* is represented by a probabilistic mixture of pure states. Therefore, it is represented by multiple outer products,

$$\rho = \sum_i p_i |\psi_i\rangle \langle\psi_i| \quad \text{where } \sum_i p_i = 1, \quad p_i \geq 0 \quad (2.4)$$

describing a state that is in  $|\psi_i\rangle$  in probability  $p_i$ . Noise, decoherence, partial knowledge of the system can cause mixed states.

Quantum states, both pure and mixed, should be represented by a density matrix  $\rho$  which is Hermitian ( $\rho = \rho^\dagger$ ), is a positive semi-definite ( $\rho \geq 0$ ), and a trace of 1 ( $\text{Tr}(\rho) = 1$ ). These conditions are necessary for  $\rho$  to describe a physically realizable quantum state.

### 2.1.2 Quantum gates

In classical computers, in order to manipulate bits that take values 0 or 1, *logic gates* such as AND, OR, and NOT are used. In the same way, in quantum computing, *quantum gates* are used to manipulate qubits. Quantum gates are represented by unitary matrices, which ensure that the quantum state preserved normalization.

#### (1) Single qubit gates

Unlike classical bits, qubits can exist in superpositions. Single qubit gates act as rotations on the Bloch sphere and are represented in  $2 \times 2$  unitary matrices.

Rotations around the three axes of the Bloch sphere are,

$$R_x(\theta) = e^{-i\frac{\theta}{2}X}, \quad R_y(\theta) = e^{-i\frac{\theta}{2}Y}, \quad R_z(\theta) = e^{-i\frac{\theta}{2}Z},$$

and rotate the state of a qubit along each axis in angle  $\theta$ . Here, the  $X, Y, Z$  are Pauli matrices defined as

$$X = \begin{pmatrix} 0 & 1 \\ 1 & 0 \end{pmatrix}, \quad Y = \begin{pmatrix} 0 & -i \\ i & 0 \end{pmatrix}, \quad Z = \begin{pmatrix} 1 & 0 \\ 0 & -1 \end{pmatrix}.$$

The Pauli gates correspond to a  $\pi$  rotation around each axis,  $X, Y, Z$ .

The  $X$  gate acts as a quantum version of classical NOT gate, it flip states:  $X|0\rangle = |1\rangle$  and  $X|1\rangle = |0\rangle$ . The  $Y$  gate combines the bit flip and phase shift:  $Y|0\rangle = i|1\rangle$  and  $Y|1\rangle = -i|0\rangle$ . The  $Z$  gate adds a phase of  $-1$  to state  $|1\rangle$ :  $Z|0\rangle = |0\rangle$  and  $Z|1\rangle = -|1\rangle$ .

The Hadamard gate creates superposition by rotating the qubit to the equator of the Bloch sphere.

$$H = \frac{1}{\sqrt{2}} \begin{pmatrix} 1 & 1 \\ 1 & -1 \end{pmatrix}$$

Thus,

$$H|0\rangle = \frac{|0\rangle + |1\rangle}{\sqrt{2}} = |+\rangle, \quad H|1\rangle = \frac{|0\rangle - |1\rangle}{\sqrt{2}} = |-\rangle.$$

## (2) Multiple qubit gates

Operations on multiple qubits can generate entanglement. One of the two-qubit gates is the *controlled-NOT (CNOT) gate*. This gate flips the state of the *target qubit*, if the *control qubit* is in state  $|1\rangle$ . The operation can be represented as,

$$\begin{aligned}\text{CNOT } |00\rangle &= |00\rangle \\ \text{CNOT } |01\rangle &= |01\rangle \\ \text{CNOT } |10\rangle &= |11\rangle \\ \text{CNOT } |11\rangle &= |10\rangle\end{aligned}$$

Here, the first qubit is the control qubit and the second qubit is the target qubit. This CNOT gate is the base for creating entangled states. For example, applying Hadamard gate to the first qubit of  $|00\rangle$  and then applying CNOT gate generates a state called a Bell state.

$$(\text{CNOT})(H \otimes I)|00\rangle = \frac{|00\rangle + |11\rangle}{\sqrt{2}} = |\Phi^+\rangle$$

This CNOT gate is denoted in a matrix form as,

$$CNOT = \begin{pmatrix} 1 & 0 & 0 & 0 \\ 0 & 1 & 0 & 0 \\ 0 & 0 & 0 & 1 \\ 0 & 0 & 1 & 0 \end{pmatrix}$$

All quantum gates are unitary, and satisfy  $U^\dagger U = I$ . Thus, quantum gates are always invertible, and the evolution can be reversed. XOR and NAND gates which are used in classical computing are irreversible or non-invertible, therefore in quantum computing we cannot introduce these gates.

### 2.1.3 Measurement and Basis

Measurement is a process where the information of a quantum state is extracted. This operation will collapse the quantum state into one of the basis states. For a single qubit state denoted as,  $|\psi\rangle = \alpha|0\rangle + \beta|1\rangle$ , when measuring the qubit in z basis, it collapses to  $|0\rangle$  or  $|1\rangle$ . The probability of outcome 0 is  $|\alpha|^2$ , the probability of outcome 1 is  $|\beta|^2$ . This corresponds to measuring along the z axis of a Bloch sphere. Unlike classical bits, the outcome of a qubit measured is probabilistic and depends on the state of the qubit and the basis the qubit is measured.

The probability of obtaining an outcome  $|i\rangle$  when measuring a state  $|\psi\rangle$  is

$$P(i) = |\langle i|\psi\rangle|^2$$

There are also other basis measurements that can be done. For example, by applying a Hadamard gate to a qubit, the measurement basis will be modified to a *X basis*.

$$|+\rangle = \frac{|0\rangle + |1\rangle}{\sqrt{2}}, \quad |-\rangle = \frac{|0\rangle - |1\rangle}{\sqrt{2}}$$

Measuring a qubit in this basis, can be represented as measuring along the  $x$  axis of the Bloch sphere.

The computational basis  $\{|0\rangle, |1\rangle\}$  is one of the ways to represent qubits. For two qubits, the computational basis consists of four states  $\{|00\rangle, |01\rangle, |10\rangle, |11\rangle\}$  and a measurement would return one of these bits.

Another standard basis for two qubits, is the *Bell basis*, which consists of four maximally entangled states  $\{|\Phi^+\rangle, |\Phi^-\rangle, |\Psi^+\rangle, |\Psi^-\rangle\}$ . Measuring in Bell basis, it can reveal correlations between entangled qubits. The details about Bell states and their application are discussed in Section 2.2.

These measurement bases are chosen based on operations you want to proceed.

## 2.2 Entanglement and Bell basis

A quantum correlation between two or more qubits, where the states of the qubits depend on the other qubits, is known as *quantum entanglement*. This is a non-classical correlation between the quantum systems, and the states of each subsystems cannot be described independently from the other [29, 16]. A pure state  $|\psi\rangle$  of two qubits is *entangled* if it cannot be factored in a tensor product of single-qubit states,  $|\psi\rangle = |\psi_A\rangle \otimes |\psi_B\rangle$ . Entanglement doesn't have a classical equivalent and is the base of quantum communication protocols.

One of the commonly used sets of entangled states are *Bell States*. These states represents a maximally entangled state.

$$|\Phi^+\rangle = \frac{1}{\sqrt{2}}(|00\rangle + |11\rangle), \quad |\Phi^-\rangle = \frac{1}{\sqrt{2}}(|00\rangle - |11\rangle)$$

$$|\Psi^+\rangle = \frac{1}{\sqrt{2}}(|01\rangle + |10\rangle), \quad |\Psi^-\rangle = \frac{1}{\sqrt{2}}(|01\rangle - |10\rangle)$$

These four Bell States form an orthogonal basis for the two qubit space known as the *Bell basis*. Therefore, any two qubit pure states can be represented by a linear combination of these states.

Bell states are essential for various quantum information protocols as quantum teleportation and quantum key distribution. In quantum networks, they are often used to generate quantum links between nodes.

## 2.3 Quantum Communication

Entanglement plays a central role in quantum communication. In quantum communication, entangled states are distributed among nodes [22]. Using entanglement as a resource, quantum communication is said to be able to perform communication that is impossible with classical resources.

### 2.3.1 Quantum teleportation

Quantum teleportation transfers arbitrary quantum states from one node (Alice) to another (Bob)[7].

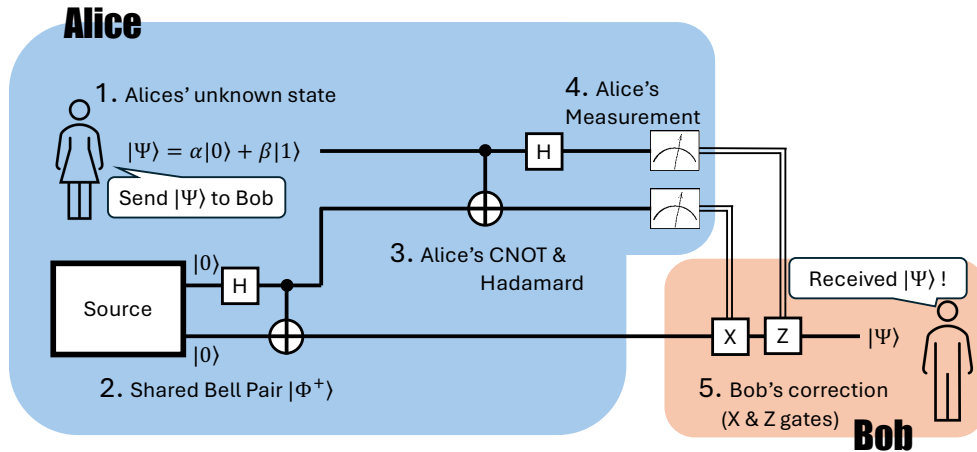


Figure 2.2: Image of figure for quantum teleportation

1. Alice has a qubit in an unknown state which she wants to teleport to Bob
2. Alice and Bob share a Bell pair
3. Alice operates a CNOT gate and a Hadamard gate on both of the qubits she has
4. Alice measures both of the qubits she has
5. Alice sends the two classical bits of measurement results to Bob
6. Bob applies a correction on his half of the entangled pair to recover the original state

### 2.3.2 Entanglement distribution and quantum repeaters

Entangled states decay when they are transmitted over optical fibers due to loss and noise. To distribute entanglement over long distances, *quantum repeaters* are used. Repeaters perform entanglement swapping, sometimes purification, and extend the entanglement over a network. Classical repeaters amplify the signals in order to transmit them with less noise. In order to amplify the signal, there is a need to know the original signal. However, for qubits used in quantum networks, the states of the qubits are unknown and the *no-cloning theorem* prevents unknown qubits from being copied and forwarded in the network.

#### No-cloning theorem

In classical communication, information can be freely copied and amplified by measuring a signal and reproducing it. In quantum mechanics, however, measuring an unknown qubit generally disturbs its state.

Quantum theory forbids the existence of any physical operation that can copy an *arbitrary unknown* quantum state. This restriction is formalized by the *no-cloning theorem*, which plays a central role in quantum communication and quantum networking.

**Proof** Assume that there exists a unitary operation  $U$  that can clone any input state  $|\psi\rangle$  using state  $|0\rangle$ :

$$U(|\psi\rangle|0\rangle) = |\psi\rangle|\psi\rangle \quad \text{for all } |\psi\rangle. \quad (2.5)$$

In this case,  $U$  must be able to clone two distinct states  $|\phi\rangle$  and  $|\varphi\rangle$ :

$$U(|\phi\rangle|0\rangle) = |\phi\rangle|\phi\rangle, \quad U(|\varphi\rangle|0\rangle) = |\varphi\rangle|\varphi\rangle. \quad (2.6)$$

Because  $U$  is unitary, it satisfies  $U^\dagger U = I$  and therefore preserves inner products. Taking the inner product of the two *input* states and using  $U^\dagger U = I$  gives

$$\langle\phi, 0|\varphi, 0\rangle = \langle\phi, 0|U^\dagger U|\varphi, 0\rangle = \langle\phi, \phi|\varphi, \varphi\rangle. \quad (2.7)$$

Since  $\langle\phi, 0|\varphi, 0\rangle = \langle\phi|\varphi\rangle$  and  $\langle\phi, \phi|\varphi, \varphi\rangle = \langle\phi|\varphi\rangle^2$ , we obtain

$$\langle\phi|\varphi\rangle = \langle\phi|\varphi\rangle^2. \quad (2.8)$$

Let  $s := \langle\phi|\varphi\rangle$ . Then  $s = s^2$ , which implies  $s \in \{0, 1\}$ . Therefore, a single unitary operation can only clone states that are either identical or orthogonal, and cannot clone arbitrary unknown quantum states.  $\square$

The no-cloning theorem explains why quantum repeaters cannot amplify unknown photonic qubits in the same way as classical repeaters.

### Entanglement swapping using Bell State Analyzers (BSAs)

One way to extend the entanglement is by using Bell State Analyzers (BSAs). The process is as follows:

1. Suppose there are three nodes, A, B and C. Entanglement is shared between node A and B, and node B and C
2. At node B, two qubits from each pair enter the BSA
3. Node B performs a Bell State Measurement (BSM), and projects the combined two qubits into one of the four Bell states
4. The qubits in node B are measured out, these operations will cause qubits at nodes A and C become entangled
5. The measurement outcome of a BSM is sent through a classical communication channel to nodes A and C, so any necessary Pauli corrections can be applied

This process of entanglement swapping is fundamental to the operations in quantum repeaters, and will enable long-distance entanglement distribution.

#### 2.3.3 Applications

Distributing the entanglement enables various applications: distributed quantum computing [12, 9], quantum key distribution [16, 6], quantum sensing [20], clock synchronization [23], etc. These applications need high quality entanglement between nodes.

## 2.4 Motivation for Integrated Photonics in Quantum Networks

Distributing entanglement for any application requires stable, scalable, and low-loss routing of photons between nodes. While bulk optics and free space fiber systems are used in laboratory research, this approach becomes troublesome for multi-node networks due to their complexity, size, and sensitivity.

Integrated photonic circuits provide a compact and stable base for implementing optical components as beam splitters, phase shifters, and switches with low optical loss [34]. This technology is key for building a scalable network in where you can route entangled photons between different nodes.

## 2.5 Fundamentals of optics for Quantum Chips

This section introduces the optical and integrated-photonics concepts needed for the photonic switch architecture studied in later chapters. We first describe a quantum-optics model of light on a chip (modes, Fock states, and single-photon qubits), then connect that description to practical qubit encodings used in quantum networks. Finally, we introduce the core building blocks of integrated interferometric circuits, waveguides, directional couplers (beam splitters), and phase shifters, and show how they combine into a Mach–Zehnder interferometer (MZI), which forms the basic  $2 \times 2$  reconfigurable switch cell.

### 2.5.1 Quantum description of light

In this thesis we treat photons as *flying qubits* that propagate through waveguides and are routed by integrated photonic components such as, directional couplers, Mach Zehnder Interferometers(MZIs). While a classical electromagnetic wave is described by a complex field amplitude, a quantum description is useful at the single-photon level, where the relevant observables are photon-number statistics and detection probabilities.

**Optical modes as communication channels** An optical *mode* is characterized by a spatial profile, polarization, frequency, and temporal envelope. In quantum optics, each mode is modeled as a quantum harmonic oscillator. Quantization replaces classical field amplitudes by operators acting on a Hilbert space, enabling a particle-like description in terms of photon number. With this mode picture, single photons and photonic qubits can be described as excitations of one or more modes.

**Single photons in practice** An ideal single photon is a one-quantum excitation of a mode. In realistic sources and detectors, photons are better described as wavepackets with a temporal mode function  $\xi(t)$ , rather than infinitely long continued waves. Interference effects used in switching and Bell-state measurements require high overlap of the photons in all degrees of freedom (spectrum, polarization, spatial mode, and arrival time).

This motivates careful control of dispersion, path-length matching, and polarization management in the photonic circuit. These requirements motivate using an operator-based description of photon number and mode transformations, introduced next.

**Creation and annihilation operators** With the mode concept in place, we can introduce operators that change the photon number in a given mode. For a single optical mode, we define the annihilation and creation operators  $\hat{a}$  and  $\hat{a}^\dagger$ , which respectively remove or add a photon in that mode. They satisfy the commutation relation  $[\hat{a}, \hat{a}^\dagger] = 1$ . The system is described in the Fock (number) basis, where  $|n\rangle$  represents a state with  $n$  photons in the mode, and

$$\hat{a}^\dagger |n\rangle = \sqrt{n+1} |n+1\rangle, \quad \hat{a} |n\rangle = \sqrt{n} |n-1\rangle. \quad (2.9)$$

The photon-number operator  $\hat{n} = \hat{a}^\dagger \hat{a}$  counts photons:  $\hat{n} |n\rangle = n |n\rangle$ . For quantum switching, we primarily operate within the single-photon subspace. A single photon in a specific mode  $k$  is represented as  $|1\rangle_k = \hat{a}_k^\dagger |0\rangle$ , where  $|0\rangle$  is the vacuum state. In a switch fabric, the relevant point is that components ideally do not create or destroy photons, but instead route them by transforming the mode operators.

**Multiple modes** Real systems involve many modes indexed by  $k$  (e.g., different waveguides, polarizations or time bins). We use operators  $\{\hat{a}_k, \hat{a}_k^\dagger\}$  satisfying

$$[\hat{a}_k, \hat{a}_\ell^\dagger] = \delta_{k\ell}. \quad (2.10)$$

A general single-photon state distributed across modes can be written as

$$|\psi\rangle = \sum_k c_k \hat{a}_k^\dagger |0\rangle, \quad \sum_k |c_k|^2 = 1, \quad (2.11)$$

which is the quantum-optics analogue of a normalized complex amplitude vector over channels. The coefficients  $c_k$  represent probability amplitudes for finding the photon in mode  $k$ . Linear optical devices, such as interferometers and switching fabrics, act by coherently redistributing these amplitudes among modes while preserving the overall normalization, enabling interference-based routing and processing of single photons. Having established how a photonic qubit can be distributed across modes, the next step is to specify which degrees of freedom carry the logical information (encoding).

**Dual-rail qubit representation** In integrated photonics, a common way to encode qubits is the dual-rail representation, where the presence of a photon in one of two modes represents the logical states:

$$|0\rangle_L = |1\rangle_a |0\rangle_b, \quad |1\rangle_L = |0\rangle_a |1\rangle_b, \quad (2.12)$$

where  $a$  and  $b$  denote the two modes. In this thesis, we assume time-bin encoding, where the qubit is represented by the presence of a photon in one of two time bins:

$$|0\rangle_L = |1\rangle_{t_0} |0\rangle_{t_1}, \quad |1\rangle_L = |0\rangle_{t_0} |1\rangle_{t_1}, \quad (2.13)$$

Polarization encoding is widely used in fiber-based quantum links, but on-chip polarization management can be challenging due to birefringence. Once a qubit is mapped to

specific modes (paths or time bins), implementing a network switch reduces to implementing reliable, low-loss transformations between those modes using integrated optical components.

### 2.5.2 Optical Waveguides

In order to modify the light through components, we need a wire that will guide the light. The light is guided inside of a chip by using *optical waveguides*. The waveguide consists of a core with a high refractive index  $n_{core}$ , surrounded by cladding with a lower refractive index  $n_{clad}$ . Light is confined in the core by total internal reflection [34]. In the context of quantum chips, the waveguide geometry must be precisely engineered to support only a single transverse mode to maintain the purity of the quantum state [34]. With guided modes provided by waveguides, the remaining building blocks must split, recombine, and phase-shift these modes to realize interference-based routing.

### 2.5.3 Directional Couplers

A directional coupler consists of two waveguides placed close together, allowing evanescent coupling of light between the waveguides [34]. This allows for splitting and combining of optical signals.

Mathematically, the operation of a lossless directional coupler can be described by a unitary transformation on the input mode operators. For two input modes  $\hat{a}_{in}$  and  $\hat{b}_{in}$ , the outputs are

$$\begin{pmatrix} \hat{a}_{out} \\ \hat{b}_{out} \end{pmatrix} = \frac{1}{\sqrt{2}} \begin{pmatrix} 1 & i \\ i & 1 \end{pmatrix} \begin{pmatrix} \hat{a}_{in} \\ \hat{b}_{in} \end{pmatrix}. \quad (2.14)$$

This transformation describes a 50:50 beam splitter, where the input light is equally split between the two output ports with a  $\pi/2$  phase shift. Directional couplers therefore serve as the on-chip analogue of beam splitters; combined with controllable phase shifts they enable programmable interference.

### 2.5.4 Phase-shifting Components

One of the key operations in integrated photonics is to apply a controlled phase shift to an optical mode. Phase control enables interference between paths and is the mechanism that makes MZI-based switches reconfigurable. For a mode propagating a distance  $L$  with effective refractive index  $n_{eff}$ , the accumulated phase is [34]

$$\phi = \frac{2\pi}{\lambda} n_{eff} L. \quad (2.15)$$

A tunable device induces a change  $\Delta n_{eff}$ , resulting in a controllable phase shift

$$\Delta\phi = \frac{2\pi}{\lambda} \Delta n_{eff} L. \quad (2.16)$$

In the quantum-optics picture, an ideal phase shifter applies the operator transformation  $\hat{a}^\dagger \rightarrow e^{i\phi}\hat{a}^\dagger$  (equivalently  $\hat{a} \rightarrow e^{-i\phi}\hat{a}$ ). Together, directional couplers and phase shifters form the two essential ingredients of an MZI.

## Thermo-optic phase shifters

Thermo-optic phase shifters use local heating to change the refractive index via the thermo-optic coefficient  $dn/dT$ . They are widely used because they are simple to fabricate and can provide a large tuning range. Speed is a trade-off in thermal devices, the switching speed has microsecond–millisecond response time and can introduce thermal crosstalk to nearby components.

## Electro-optic phase shifters

Electro-optic phase shifters use an applied electric field to change the refractive index. In materials with a strong electro-optic effect, this enables fast phase control with reduced thermal crosstalk. Electro-optic phase shifters typically require dedicated electrode structures and a suitable material platform.

### 2.5.5 Mach-Zehnder Interferometer (MZI)

An MZI consists of two beam splitters (directional couplers) connected by two arms, with a phase shifter placed in one (or both) arms. The first coupler splits the input field into the two arms, the phase shifter creates a relative phase difference, and the second coupler recombines the fields. Depending on the relative phase, interference at the second coupler directs the light to one output port or the other [34].

For the 50:50 coupler convention used in the previous subsection,

$$\begin{pmatrix} \hat{a}_{\text{out}} \\ \hat{b}_{\text{out}} \end{pmatrix} = U_{\text{MZI}}(\phi) \begin{pmatrix} \hat{a}_{\text{in}} \\ \hat{b}_{\text{in}} \end{pmatrix}, \quad U_{\text{MZI}}(\phi) = C \text{ diag}(e^{i\phi}, 1) C, \quad (2.17)$$

where  $C$  is the 50:50 coupler matrix. Up to an irrelevant global phase, this gives a tunable  $2 \times 2$  unitary transformation controlled by  $\phi$ . For example, when light enters only one input port, the output powers vary as

$$P_{a \rightarrow a}(\phi) = \sin^2\left(\frac{\phi}{2}\right), \quad P_{a \rightarrow b}(\phi) = \cos^2\left(\frac{\phi}{2}\right), \quad (2.18)$$

so that tuning  $\phi$  switches continuously between the two outputs. With this convention,  $\phi = 0$  routes input  $a$  to output  $b$  (CROSS), while  $\phi = \pi$  routes input  $a$  to output  $a$  (BAR). In practice, the achievable switching contrast is limited by coupler imbalance, propagation loss mismatch between arms, and imperfect phase control.

MZIs form the core of reconfigurable optical switches: by controlling  $\phi$ , an MZI implements a programmable  $2 \times 2$  switch cell. Larger switching fabrics can then be constructed by cascading many such cells. Because an MZI implements a tunable  $2 \times 2$  unitary on a pair of modes, later chapters evaluate switch performance primarily through MZI-level metrics such as insertion loss, extinction ratio, and phase-setting robustness, and then extend these results to larger switching networks.

## 2.6 Noise in Quantum systems

Noise and imperfections reduce the quality of quantum states and the success probability of entanglement distribution. In photonic quantum networks and integrated switches, the dominant effects are typically optical loss, phase noise, and mode mismatch. These errors are especially important for Bell-state measurements (BSMs), which rely on high-visibility interference between indistinguishable photons.

### 2.6.1 Photon loss and insertion loss

Photon loss can occur in propagation, bends, couplers, crossings, and at chip-to-fiber interfaces. A standard quantum-optics model represents loss as coupling to an unobserved vacuum mode  $\hat{v}$  via a beam splitter of transmissivity  $\eta$ :

$$\hat{a}_{\text{out}} = \sqrt{\eta} \hat{a}_{\text{in}} + \sqrt{1 - \eta} \hat{v}. \quad (2.19)$$

For a single-photon state,  $\eta$  is the probability that the photon is transmitted (and  $1 - \eta$  that it is lost). When multiple components are cascaded, the overall transmission is approximately the product of the individual transmissions,  $\eta_{\text{tot}} \approx \prod_i \eta_i$ . The corresponding insertion loss is often reported in dB as  $\text{IL} = -10 \log_{10}(\eta_{\text{tot}})$  [34].

### 2.6.2 Phase noise and stability

Phase fluctuations arise from temperature drift, electrical noise, and fabrication variations. If the intended phase is  $\phi_0$  but the applied phase is  $\phi = \phi_0 + \delta\phi$ , then interference fringes are reduced. For small random fluctuations  $\delta\phi$  (e.g., approximately Gaussian with variance  $\sigma_\phi^2$ ), the interference visibility is suppressed by a factor that scales roughly as  $\exp(-\sigma_\phi^2/2)$ . In switching fabrics, phase stability and calibration therefore directly impact switching contrast and long-term reliability.

### 2.6.3 Mode mismatch and distinguishability

High-visibility interference requires the two photons entering a BSM to be indistinguishable in all degrees of freedom: spectrum, polarization, spatial mode, and arrival time. For temporal modes described by normalized wavepackets  $\xi_1(t)$  and  $\xi_2(t)$ , a useful overlap parameter is

$$\gamma = \int dt \xi_1^*(t) \xi_2(t), \quad 0 \leq |\gamma| \leq 1. \quad (2.20)$$

The interference visibility is reduced as distinguishability increases, and ideal interference requires  $|\gamma| \approx 1$ . This motivates tight timing synchronization, low-dispersion routing, and careful control of polarization and mode profiles.

### 2.6.4 Impact on entanglement distribution

Loss reduces entanglement generation rates because many attempts result in no detections. Imperfect interference (from phase noise and mode mismatch) reduces the fidelity of the

generated entangled state and can increase the error rate of entanglement swapping. For this reason, later chapters evaluate switch performance using metrics such as insertion loss, switching contrast (extinction ratio), and interferometric behavior of the  $2 \times 2$  MZI switch cell.

## Chapter 3

# Structure of Quantum Interconnects

### 3.1 System model of the Quantum Network

The optical switches designed in this thesis are intended to operate as a reconfigurable routing layer in a quantum network. Existing quantum network proposals differ widely in the assumed hardware platforms, network topologies, and target applications. To avoid ambiguity and to connect this work to the broader landscape of *quantum interconnect* architectures, this chapter specifies the system model assumed throughout the thesis and summarizes representative proposed architectures that rely on optical switching. By comparing these architectures, we clarify what kinds of optical switches (port count, loss budget, reconfiguration capability, and path-length symmetry) are required for scalable entanglement distribution. Particularly, the network considered in this thesis consists of stationary qubits stored in ion-trap nodes, photonic flying qubits that propagate through optical channels, and intermediate measurement and routing elements, such as Bell-state analyzers(BSAs) and optical switching fabrics.

#### 3.1.1 Network component and interfaces

**Quantum nodes** A quantum node is a device used to store and process quantum information using stationary qubits. Various physical platforms can realize such nodes, as trapped ions, superconducting qubits, neutral atoms. Each have different trade-offs as coherence time, gate fidelity, and system complexity. In this thesis, ion traps are assumed as end nodes due to their long coherence times and suitability to quantum memories. Each node is assumed to contain one or more trapped-ion qubits that will be used as stationary storage for entanglement generated in the network.

**Matter-photon interface** While stationary qubits are good for storage and local operations, they are not practical for long distance communication. In order to use ion-traps as qubits, it requires a controlled environment using vacuum systems and stabilized lasers. This makes the direct transmission of matter qubits not practical. Thus, for inter-node

communication, the network is assumed to use photonic flying qubits. The interface between stationary ion qubits and photonic flying qubits is realized by an ion-photon entanglement generation process. When an ion is excited and emits a photon, the ion's internal state can become entangled with a photonic degree of freedom, as polarization, frequency, and time-bin. In this system model we assume that photons generated from exciting ions, are collected and coupled into an optical channel, such as fiber and on-chip waveguide. This enables the transfer of entangled photon from a node into the network. The details of ion-photon entanglement generation is introduced in Sec 5.2.1

**Flying qubits** Flying qubits are photons that carry quantum information through optical links and devices. Photons are suited as signals sent through the network since they can propagate over long distances with relatively low decoherence and are compatible with devices currently used in classical networks as fibers. In this thesis, flying qubits are treated as network signals that are routed by optical switching fabric and measured in BSAs to establish entanglement between remote ion-trap memories. The way to encode photons, as polarization, time-bin, determines practical requirements for the network, as polarization management, timing synchronization, and will be discussed in Sec 3.1.3.

**Bell State Analyzer** In quantum network, to be able to do applications between nodes, many tasks require entanglement between stationary qubits located at different nodes. A method to establish such entanglement is to interfere two photons and perform a Bell State measurement, which generates entanglement between remote pairs. Bell state measurements enables *entanglement swapping*, which converts entanglement from stationary-flying pair to stationary-stationary entanglement and can be used to extend entanglement across multiple network segments. In this thesis, the device performing this measurement is referred to as a Bell state analyzer(BSA). The measurement operation is described in Sec 2.3.2.

**Optical switching fabric** As the number of nodes increases, a reconfigurable routing layer will be needed to connect different node pairs to available BSAs, to scale up simple grid network. The optical switching fabric provides this functionality by routing flying qubits to different destinations, either toward a selected BSA for entanglement generation and swapping, or toward the additional switching layers in a larger multi hop topology. Optical switch is important since in quantum networks, quantum states cannot be copied or amplified without disturbing the encoded information, because of the non-cloning theorem. Thus, the lossy transmission cannot be mitigated in the same way as classical style signal amplification, and the network will have to rely on operation as Bell state measurement, to be able to share entanglement between remote nodes. The switch fabric will enable efficient sharing of a limited number of BSAs among many nodes, flexible pairing of nodes depending on the network demand and resource availability, and construction of larger switching architectures by interconnecting multiple switching stages.

**Classical control plane** To coordinate operations, the network requires a classical control plane. Classical messages are used to distribute heralding outcomes from BSAs,

apply feed-forward operation at the end nodes, and schedule and configure the optical switch states to route signals based on desired end-to-end entanglement. In the system model assumed here, classical communication is available between all relevant systems, as nodes, switch and BSAs, and the switching fabric is controlled in real time based on the selected pairing strategy and measurement outcomes.

### 3.1.2 Operation flow

The core operation considered in this thesis is the heralded generation of entanglement between two remote ion-trap memories using two photons and a BSA. A typical attempt to generate entanglement is as follows,

1. **Ion-photon entanglement at each node**

$$|\Psi\rangle_{Aa} = \frac{1}{\sqrt{2}} (|0\rangle_A |H\rangle_a + |1\rangle_A |V\rangle_a), \quad |\Psi\rangle_{Bb} = \frac{1}{\sqrt{2}} (|0\rangle_B |H\rangle_b + |1\rangle_B |V\rangle_b), \quad (3.1)$$

where  $a$  and  $b$  denotes the emitted photons, and  $A$  and  $B$  denotes the stationary qubits.

2. **Routing through switching fabrics** The two photons are injected to the optical network and routed by the switch to arrive to the same BSA input. In larger, architectures, photons may travel multiple switch stages before reaching the same BSA.
3. **Two photon interference and Bell state measurement** The BSA will interfere photons  $a$  and  $b$  and measures them using single - photons detectors.
4. **Heralded projection to memory-memory entanglement** When there is a successful detection outcome, the joint state of the remote ions is projected into an entangle state. The BSA will project the photonic subsystem onto a Bell state  $|\beta\rangle$ ,

$$|\Psi\rangle_{AB} \propto (\langle \beta |_{ab}) (|\Psi\rangle_A \otimes |\Psi\rangle_B), \quad (3.2)$$

producing a corresponding entangled state between ions  $A$  and  $B$ .

5. **Classical heralding and Pauli frame update** The BSA measurement outcome will be communicated classically. Depending on the measured Bell state, some kind of Pauli correction may be required.

These procedures demonstrate what happens to specifically two qubits that are generated and sent out to the network by nodes that want to share an entanglement.

### 3.1.3 Timing and synchronization

Successful Bell state measurements require high visibility two photon interference, which requires timing constraints on photon generation, routing, and arrival at the BSA. The key requirement is that the two photons overlap in time ar the BSA, within the coherence time of their wavepackets.

**Wavepacket overlap condition at the BSA** Let the temporal mode of a photon arriving at the BSA be described by a normalized wavepacket  $\xi(t)$ , such that the creation operator for that temporal mode is

$$\hat{a}_\xi^\dagger = \int dt \xi(t) \hat{a}^\dagger(t), \quad \int dt |\xi(t)|^2 = 1. \quad (3.3)$$

If the two photons arrive with a relative delay  $\Delta\tau$ , their temporal overlap is quantified by

$$\Lambda(\Delta\tau) = \left| \int dt \xi^*(t) \xi(t - \Delta\tau) \right|^2. \quad (3.4)$$

High visibility interference requires  $\Lambda(\Delta\tau) \approx 1$ , which is achieved when  $|\Delta\tau|$  is much smaller than the wavepacket duration. When  $|\Delta\tau|$  becomes comparable to the wavepacket length, interference visibility degrades and the fidelity of the heralded remote entanglement decreases.

**Timing for Time-bin** For time-bin encoding, the photonic qubit is encoded in two temporal modes, *early* and *late*, separated by  $\Delta t$ . When using time-bin encoding, we must ensure that the corresponding bins from two photons overlap. The early-early and late-late interference should be aligned. This requires controlling the path length so that the delays between the two network paths are stable within the coherence time of the photons.

**Network level synchronization and memory waiting time** Entanglement generation is probabilistic, thus, successful generation event occur at random times. Quantum memories allow the network to keep successful entangled states. This creates a constraint that the memory coherence time must be longer than the expected waiting time.

**Balanced switching depth for photons entering the same BSA** One of the components that may introduce a delay between two photons is switches. If one photons travels through more switches than the other, it may experience delay and dispersion, reduce temporal overlap as introduced by Eq. (3.4). Therefore, switch network designs that produce path length symmetry are advantageous for maintaining stable Bell state measurement performance.

### 3.1.4 Representative interconnect topologies

Network topology describes how quantum nodes, switches, and BSAs are connected. Different topologies determine the required switch port count, number of switching stages a photon will pass, and how BSAs are shared among users. This section introduces some proposed topologies for quantum network discussions and summarizes what each topology implies for optical switching fabric.

#### (1) Repeater chain topology

The simplest building block of links in quantum network is a *elementary link*. Two end nodes can share entanglemnt using photons and a BSA. A typical realization is shown as:

$$\text{Node } A \rightarrow (\text{photon}) \rightarrow \text{BSA} \leftarrow (\text{photon}) \leftarrow \text{Node } B.$$

An successful measurement at the BSA heralds entanglement between the memories at  $A$  and  $B$ . To extend entanglemnt over longer distances, multiple elementary links can be connected and form a *repeater chain*.

In a repeater chain, the routing task is structured since each photon must be routed to the correct BSA in the neighboring node, causing the switch to have less depth. However, the timing requirement becomes stricter as multiple links must have successful BSA measurement within the memory coherence time.

## (2) Multicomputer interconnect

A different approach is to connect many end nodes to a central station that contains a pool of BSAs and switches. Any chosen pair of nodes can attempt entanglement by routing their photons to the same BSA. This architecture's highlight is that by sharing BSAs, we can reduce the numbers of BSAs, which reduces cost and maintenance difficulty.

For larger networks, a single hub can become a bottleneck in port count and loss. A common scalable alternative at the architecture level is to interconnect multiple switching domains, so that photons may traverse more than one switch block before reaching a target BSA. In contrast, how a large  $N \times N$  switch is physically realized inside one switch domain, for example by composing many smaller  $S \times S$  elements into multiple internal stage, is a switch-design decision and is treated later in this thesis rather than as a separate architecture motif here.

**Switched shared-BSA-pool interconnect (pair-to-BSA routing)** One of the used architectural motifs for near-term quantum interconnects is to centralize expensive measurement hardware while keeping quantum memories distributed at the edge: end nodes generate matter–photon entanglement locally, then route the photonic qubits through an optical switching fabric to a *shared pool* of Bell-state analyzers (BSAs) as shown in Fig. 3.1. Successful Bell-state measurement outcomes herald remote memory–memory entanglement, enabling applications such as distributed quantum computing and networked sensing. In this model, the switching fabric must solve a *pairing* problem: for any requested set of disjoint node pairs, it must route the two photons of each pair to the same BSA (often to adjacent input ports of a BSA) while avoiding conflicts. This thesis adopts this model as the primary use case, and later chapters focus on planar, low-loss realizations appropriate for integrated photonics and MZI-based switch points [25, 13].

**Modular quantum computer interconnects (photonic links between QPUs)** Optical interconnects also appear in proposals for *modular* quantum computing, where many small processor modules (e.g., ion-trap or other matter-qubit modules) are linked by photonic entanglement. A canonical architecture uses reconfigurable optical networking to connect elementary logic units (ELUs) and to create entanglement between arbitrary module pairs as needed for distributed algorithms [28]. As the number of modules grows to a data-center scale, the interconnect is often organized as a *fabric* rather than a single central switch. Two representative motifs are: (i) *hierarchical fabrics* inspired by classical

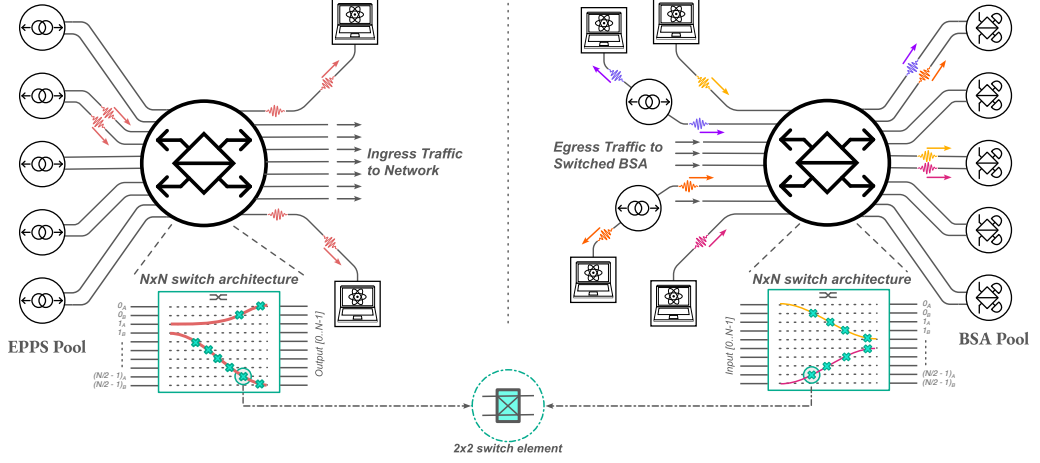


Figure 3.1: Shared-BSA-pool and Shared-EPPS-pool interconnect

Left: A switching network using Entangled Photonic Pair Source (EPPS) to distribute entanglement between QPUs. Right: A central switch dynamically routes selected node pairs to a limited pool of BSAs.

data-center networks (e.g., fat-tree-like topologies), where QPUs connect to top-of-rack (ToR) switches and higher tiers provide multi-hop connectivity across racks [36]; and (ii) *group-based low-diameter fabrics* such as Q-Fly, where QPUs attach to group switches and inter-group links provide scalable global connectivity [33]. Figure 3.2 illustrates both at a schematic level. For these architectures, the interconnect switch must support dynamic many-to-many connectivity and scheduling, while maintaining indistinguishability constraints (timing, polarization, spectral alignment) required for high-visibility interference. Compared to a single-hop star, the key architectural parameter is the number of *switch domains / tiers* traversed per photon (multi-hop switching), which directly impacts the end-to-end loss and timing skew budget.

**Heterogeneous and multi-degree-of-freedom interconnects** Practical quantum networks may need to support heterogeneous encoding formats (polarization, time-bin, phase, frequency) and multiple protocol families as shown in Fig. 3.3. Recent experimental work demonstrates multi-protocol and multi-degree-of-freedom switching in a single network, highlighting that interconnect control may involve both optical-path reconfiguration and protocol/encoding translation at the edge [27].

### 3.1.5 Architectural implications for switch requirements

The architectural patterns above translate into requirements on the optical switching fabric. In this thesis we focus on integrated, planar, scalable switch networks built from modular  $M \times M$  elements, so the following requirements are framed in terms of what the switch must guarantee to support heralded two-photon interference at a shared BSA pool.

**Connectivity objective: pair-to-BSA routing** The interconnect must route any requested set of disjoint node pairs to a limited pool of BSAs. Depending on the BSA

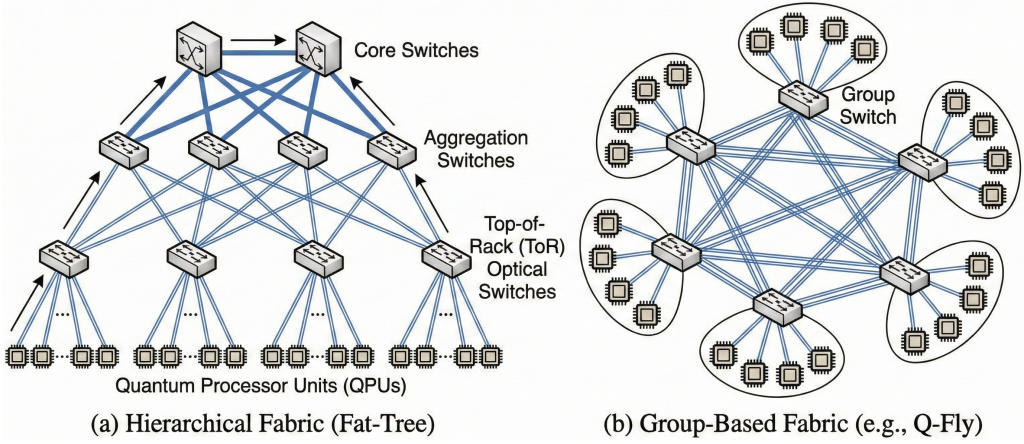


Figure 3.2: Modular quantum computer interconnect motifs that rely on optical switching  
(a) Hierarchical data-center-style fabric (fat-tree-like), where ToR/aggregation/core tiers provide connectivity and may host shared measurement resources. (b) Group-based fabric (Q-Fly-like), where QPUs attach to group switches with local BSA pools and groups are connected by inter-group links.

hardware, this may require the two photons to arrive at *adjacent* ports (paired-egress constraint) or at a specified output ordering.

**Low loss and bounded depth** Because quantum states cannot be amplified and loss directly reduces heralding rates, the dominant objective is typically minimizing insertion loss. For architectures that route photons through multiple switch *domains* (multi-hop switching), this motivates limiting the number of switching elements traversed per photon (effective depth) and preferring designs with a provably minimal number of active switch points for the pairing problem.

**Path-length symmetry and timing control** High-visibility interference requires temporal overlap at the BSA (Section 3.1.3). Therefore, architectures and routing algorithms that keep path lengths balanced between two photons in the same entanglement attempt are advantageous. In practice, this can be addressed by symmetric network topologies, matched waveguide lengths, and/or explicit delay compensation.

**Encoding compatibility (polarization vs. time-bin)** Switch requirements depend on how the photonic qubit is encoded. Polarization encoding requires components maintaining the polarization or active compensation, whereas time-bin encoding requires preserving relative delays between early/late modes and stable interferometric phases. The chip-level designs in later chapters target time-bin-friendly integrated photonics, where the switch should be phase-stable and avoid path-dependent dispersion.

**Control plane and reconfiguration timescale** The switch must be reconfigured on a timescale compatible with entanglement generation attempts and scheduling. Thermo-optic phase shifters offer mature integration but can be slow; electro-optic approaches can

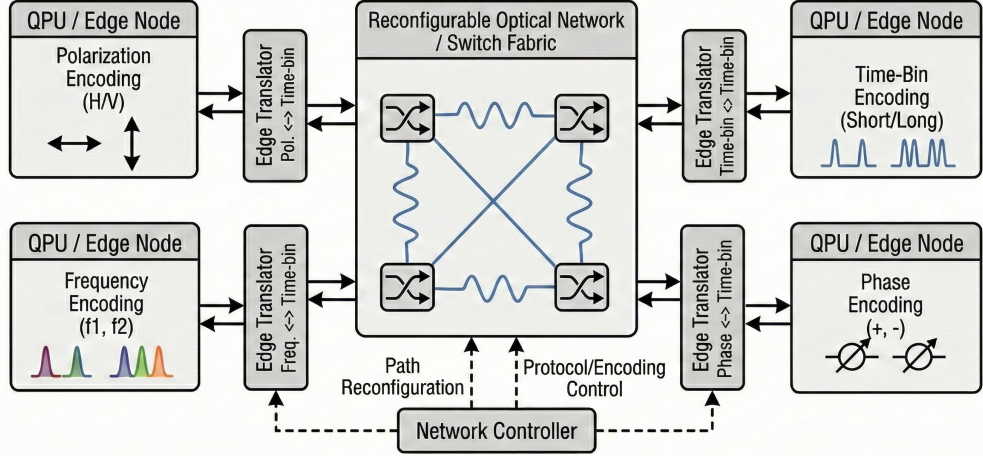


Figure 3.3: Heterogeneous interconnect

Nodes using different photonic encodings (polarization, time-bin) connect through adapters to a shared switching fabric that routes photons to BSAs and protocol modules. AI tools were used in making this figure.

Table 3.1: Representative quantum interconnect architectures and the corresponding implications for optical switching fabrics.

Architectures	Switch implications
Shared BSA pool (pair-to-BSA routing)	Pairing routability; often paired-egress constraint; minimize loss and number of switch points; fast classical orchestration.
Modular QPU/Q-node interconnect	Dynamic many-to-many connectivity; scheduling-aware reconfiguration; preserve indistinguishability for interference across modules.
Heterogeneous / multi-DoF switching	May require encoding-aware switching, interface modules, and control-plane support for protocol translation and synchronization.

be faster but may impose different fabrication and drive constraints. The appropriate choice depends on whether the interconnect is reconfigured per attempt, per time-bin frame, or on longer scheduling epochs.

## Chapter 4

# Optical switching design for Quantum Interconnects

### 4.1 Overview of Optical switching

This chapter defines the switching fabric problem and presents network level designs that meet the required connectivity for entanglement distribution between nodes. I consider a network with  $N$  input channels, where any selected pair of photons must be routed to the same BSA ports. Because a limited number of BSAs can be installed in practice, the switch fabric must be able to dynamically connect arbitrary input pairs to a shared pool of BSAs.

**Non-blocking and rearrangeably non-blocking.** In this thesis, *non-blocking* means that for any valid pairing request, there exists a switch configuration that can connect every requested pair to the BSA pool *simultaneously* without preventing any other requested pair from being realized. A fabric is *rearrangeably non-blocking* if it can realize every pairing request, possibly by *rearranging* (reconfiguring) the switch settings between different requests.

**Design target.** The main design target is to minimize the number of  $M \times M$  switches used in a planar layout, while keeping the non-blocking property. I also aim to minimize the depth in the design, achieving balanced depth among inputs to reduce loss imbalance.

**Assumptions.** I assume ideal switching functionality as that, each  $M \times M$  switch can implement an arbitrary permutation between its inputs and outputs. Physical imperfection as, insertion loss, extinction ratio, fabrication constraints, are abstracted into per element parameter and quantified in Chapter 6 through device level simulation.

### 4.2 Switching Notations and Performance Metrics

An  $N \times N$  fabric denotes a network with  $N$  input channels and  $N$  output channels as in Figure 4.2.

I construct the fabric from identical  $M \times M$  switching elements. The fabric depth  $D$  is defined as the maximum number of switch elements traversed by any input – output path in the network.

To connect architectural choices to physical feasibility, I track:

- **Insertion loss(IL):** per element loss  $IL_{sw}$  and total path loss  $IL_{path} \approx \sum_{j=1}^D IL_{sw,j}$ .
- **Extinction / crosstalk:** finite extinction ratio causes leakage into unintended ports.
- **Balanced depth:** for two photon interference, the two photons entering the same BSA should experience similar loss and similar phase noise. I therefore prefer designs with bounded depth spread, i.e.,  $\max D - \min D$  small across all input-to-BSA routes.

In Chapter 6, I quantify  $IL_{sw}$  and extinction ratio for specific photonic implementations and use those values to estimate end-to-end system performance.

### 4.3 Existing Switching Architecture

A full crossbar, illustrated in Figure 4.1(a), implements arbitrary connectivity but scales poorly because it requires  $\mathcal{O}(N^2)$  switching complexity and implies large control overhead. Classical multistage networks, such as the Benes architecture shown in Figure 4.1(b), reduce complexity by composing small-radix elements across multiple stages, often achieving rearrangeable or non-blocking behavior with  $\mathcal{O}(N \log N)$  switches.

Classical multistage networks aim to route all input signals to distinct, arbitrary output ports. In contrast, quantum networks often require routing arbitrary pairs of signals to the same Bell State Analyzer (BSA). Since the destination is a shared pool rather than a specific output port, the conditions for non-blocking behavior are relaxed, potentially allowing for a reduction in the total number of switches.

Regarding switching networks specifically optimized for quantum applications, there are currently limited studies. Most existing works, such as [38] and [25], assume the use of  $2 \times 2$  switches to create an  $N \times N$  fabric. However, since modern integrated photonics allows for fundamental building blocks larger than  $2 \times 2$  (e.g.,  $3 \times 3$  or  $4 \times 4$ ), this thesis explores these higher-radix designs to improve scalability.

### 4.4 Minimal switch count for planar pair-to-BSA routing

In this section, I derive the minimal number of  $M \times M$  switching elements required by a *planar* non-blocking fabric that supports *pair-to-BSA* connectivity. The fabric must route any pairing of  $N$  input channels to a pool of  $N/2$  Bell-state analyzers (BSAs), where each BSA consumes two output ports.

#### 4.4.1 Problem setting and worst-case pairing

Let the  $N$  input ports be  $\{X_0, \dots, X_{N-1}\}$ . A pairing request specifies  $N/2$  disjoint pairs  $\{(X_{a_1}, X_{b_1}), \dots, (X_{a_{N/2}}, X_{b_{N/2}})\}$ . To bound the required switching resources, I consider

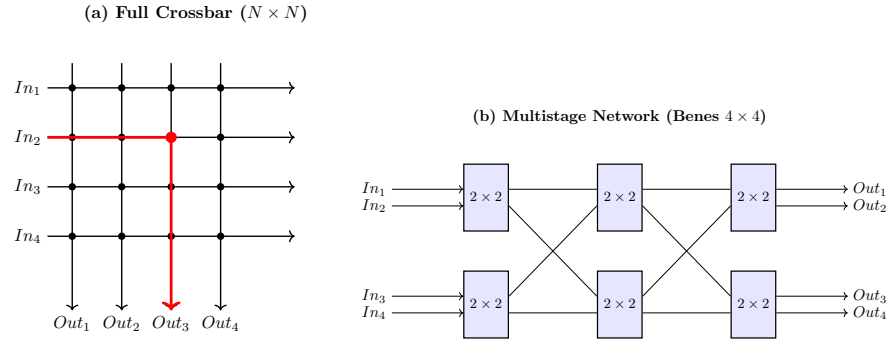


Figure 4.1: Existing switching architectures for quantum networks.

- (a) A full crossbar switch offers non-blocking connectivity but requires  $N^2$  crosspoints. (b) A multistage Benes network reduces complexity to  $\mathcal{O}(N \log N)$

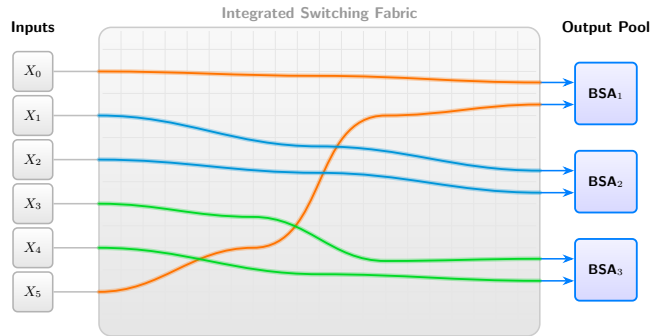


Figure 4.2: Overview of the optical switching architecture.

The fabric must dynamically route arbitrary pairs of input photons (represented by matching colors) to a shared pool of Bell State Analyzers (BSAs). Note that the fabric must handle both adjacent pairs (e.g.,  $(X_1, X_2)$ ) and distant pairs (e.g.,  $(X_0, X_5)$ ) simultaneously without blocking.

the worst-case pairing pattern that maximizes the distance between the pairs in the planar ordering:

$$(X_0, X_{N-1}), (X_1, X_{N-2}), \dots \quad (4.1)$$

The goal is to bring each such pair to adjacent outputs, and then to the same BSAs, using the fewest  $M \times M$  switches.

#### 4.4.2 Parity and termination at two channels

Each reduction layer resolves an integer number of pairs and therefore removes an even number of channels. Hence, the parity of the unresolved size is preserved across layers. In the pair-to-BSA setting we assume  $N$  is even (there are  $N/2$  disjoint pairs), so the reduction can always terminate at exactly two remaining channels. We therefore fix the terminal size to

$$n_{\text{stop}} := 2. \quad (4.2)$$

The final reduction layer may be partially filled (extracting fewer than  $(M - 1)$  pairs), which corresponds to using an  $M \times M$  element with some unused ports in that last layer.

#### 4.4.3 Layer-wise reduction argument

**Step 1: First-layer reduction.** In the first layer, the  $(M - 1)$  most distant pairs can be made adjacent by arranging  $(N - M)$  switches so that

$$(X_0, X_{N-1}), \dots, (X_{M-2}, X_{N-(M-1)})$$

become neighboring at the layer output. After resolving these  $M - 1$  pairs, the remaining unresolved sub-network contains

$$N - 2(M - 1)$$

inputs.

**Step 2: Recursive reduction and number of layers.** The same construction applies recursively to the remaining unresolved sub-network. After  $i$  completed layers, the number of unresolved inputs is

$$N - 2(M - 1)i.$$

Reduction continues until the unresolved size reaches the terminal size  $n_{\text{stop}} = 2$ . Hence, the number of required reduction layers is

$$L = \left\lceil \frac{N - 2}{2(M - 1)} \right\rceil. \quad (4.3)$$

**Step 3: Switch count per layer and total count.** In layer  $i$  (with  $i = 0, \dots, L - 1$ ), the unresolved region has size  $N - 2(M - 1)i$ , and the planar construction uses

$$[N - 2(M - 1)i - M]$$

switches to perform the next reduction. As in the first layer,  $(N - M)$  switches are needed to route  $2(M - 1)$  signals. Summing over layers gives the total number of  $M \times M$  switches:

$$\begin{aligned} S(N, M) &= \sum_{i=0}^{L-1} [N - 2(M - 1)i - M] \\ &= L(N - M) - (M - 1)L(L - 1). \end{aligned} \quad (4.4)$$

**Step 4: Partial final layer.** When  $(N - 2)/[2(M - 1)]$  is not an integer, the last reduction layer extracts fewer than  $(M - 1)$  pairs. Let

$$n_{\text{last}} := N - 2(M - 1)(L - 1)$$

be the unresolved size at the input of the final layer. In that last layer, the number of extracted pairs is

$$q_{\text{last}} := \frac{n_{\text{last}} - 2}{2},$$

which satisfies  $0 \leq q_{\text{last}} \leq M - 1$  by the definition of  $L$ . This leaves exactly two channels unresolved (already adjacent) for assignment to the remaining BSA port pair, and may leave some switch ports unused in the final layer.

#### 4.4.4 Result and consistency check for $M = 2$

Combining Eqs. (4.2), (4.3), and (4.4), the switch count for the planar pair-to-BSA construction is

$$S(N, M) = L(N - M) - (M - 1)L(L - 1), \quad L = \left\lceil \frac{N - 2}{2(M - 1)} \right\rceil, \quad n_{\text{stop}} = 2. \quad (4.5)$$

For  $M = 2$ , Eq. (4.3) gives  $L = (N - 2)/2$  (for even  $N$ ). Substituting into Eq. (4.4) yields

$$S(N, 2) = \frac{N(N - 2)}{4}, \quad (4.6)$$

which matches the known minimal count for the  $2 \times 2$  planar architecture used in prior work.

## 4.5 Design and routing

In this section, I present several rearrangeably non-blocking, acalable, planar layouts that achieve the minimal switch count  $S(N, M)$  derived in Sec. 4.4. All layouts described in this section are also recursive (shape-preserving), as after routing a batch of pairs to adjacent BSA ports and fixing the corresponding switch settings, the remaining unused fabric can be redrawn as a smaller instance of the same layout. This recursion gives both an inductive argument for rearrangeable non-blockingness and a constructive routing method.

Unless otherwise stated, I consider designs where the same number of pairs is extracted in every reduction layer. Let  $q$  denote this per-layer extraction capacity in pairs. Since one layer can extract at most  $(M - 1)$  pairs, we have

$$1 \leq q \leq M - 1. \quad (4.7)$$

If every layer extracts exactly  $q$  pairs and there is no partially filled last layer, then the network size must satisfy

$$\frac{N-2}{2q} \in \mathbb{Z} \quad (\text{equivalently, } N = 2 + 2qL \text{ for some integer } L). \quad (4.8)$$

For example, with  $q = 2$  the realizable sizes increase in steps of +4 per additional recursive layer.

More generally, different layers may use different capacities (e.g., mixing  $q = 1$  and  $q = 2$  layers within one fabric). Such designs can realize additional values of  $N$  while preserving non-blockingness and the minimal switch count.

The switching fabric is denoted as squares connected to  $M \times M$  straight waveguides, ordered from top to bottom as  $X_0, \dots, X_{N-1}$ . A routing request is a set of pairs  $\{(X_{a_1}, X_{b_1}), \dots, (X_{a_{N/2}}, X_{b_{N/2}})\}$ , and the fabric must map each pair to adjacent output ports that feed the same BSA.

To illustrate the recursive reduction, I also show a  $2 \times 2$  instance with  $N = 10$  inputs for each layout. Because  $M = 2$  implies a per-layer extraction capacity of  $q = M - 1 = 1$ , each reduction step resolves one pair and reduces the unresolved size by two.

#### 4.5.1 Routing principle

All layouts follow the same recursive reduction principle, where each reduction layer extracts up to  $(M - 1)$  pairs (i.e.,  $2(M - 1)$  photons) by making the two photons of each extracted pair adjacent at the layer output, and the remaining unresolved region shrinks until only two channels remain.

Routing within each layer is performed by,

1. **Select pairs to extract in the current layer.** Choose up to  $(M - 1)$  signals which lie in the bottom of the unresolved region.
2. **Configure the switches in the layer to make each selected pair adjacent.** Because each  $M \times M$  element is an arbitrary permutation, the layer of switches can route the signals until each pair is transported to two neighboring waveguides.
3. **Assign adjacent outputs to BSAs and remove extracted signals.** The extracted adjacent pairs are connected to the same BSA port. The remaining signals form a smaller instance of the same problem.

This matches the reduction count argument in Sec. 4.4 and achieves  $S(N, M)$ .

**Unified pair-removal recursion routing.** Although the drawings of the suggested design layouts look different, they use the same routing logic. In each reduction layer, we repeatedly take the bottom-most unresolved photon and its partner, first pushing the partner as far downward as possible using the earliest available switch interactions, and then (if needed) pushing the bottom-most photon upward using latest available switches so that the two photons meet on adjacent output lines. We commit the corresponding switch states, remove the resolved adjacent pair, and repeat this procedure  $q$  times in the

layer. After extracting  $q$  pairs, the remaining unused fabric is isomorphic to a smaller instance of the same layout, so the same step recurses until only two channels remain.

#### 4.5.2 Recursive designs

Several planar layouts can be designed recursively. After committing switch settings that route a small batch of pairs to adjacent BSA ports, the remaining unused portion of the fabric can be redrawn as a smaller instance of the same layout.

This layout design method is useful in two ways. First, it gives a compact proof for rearrangeable non-blocking property via induction on the number of unresolved channels. Second, it provides a constructive routing method which routes  $Q$  pairs, remove the used region, and repeats on the unused switches.

Throughout this section, let the current unresolved size be  $n$  (initially  $n = N$ ). In one recursive step we extract  $Q$  disjoint pairs, where

$$1 \leq Q \leq M - 1, \quad (4.9)$$

and forward the resulting  $Q$  adjacent output pairs to the BSA pool.

In the following, I present four recursive layouts: (i) triangular layout, (ii) pizza slice layout, (iii) a chevron layout, and (iv) a brickwork layout.

##### (1) Triangular layout

The *triangular* layout is the most direct planar realization of the reduction construction, and it is also shape-preserving under recursion. After each layer extracts a batch of pairs at the boundary and those paths are removed, the remaining unused switch-point pattern is isomorphic to a smaller triangular instance.

Geometrically, the active switch region shrinks by  $2q$  channels per layer when extracting  $q$  pairs, so the boundary of the active area forms a triangular outline.

**Extraction capacity and depth trade-off.** In a triangular fabric built from  $M \times M$  switches, a single diagonal switching chain can extract between  $q = 1$  and  $q = M - 1$  pairs to adjacent outputs. We call  $q$  the *per-layer extraction capacity*.

Varying  $q$  does not contradict the minimal switch count result of Sec. 4.4. Changing  $q$  corresponds to redistributing the same set of required  $M \times M$  elements across more (or less) chains. Figure 4.3 shows two triangular designs for  $N = 12$  using  $3 \times 3$  switches. One design extracts  $q = 2$  pairs per stage and completes routing in three stages, while the other extracts  $q = 1$  pair per stage and therefore requires more stages, while preserving the same non-blocking functionality and total switch count. Moreover, different capacities can be combined within one design (e.g., some layers with  $q = 2$  and others with  $q = 1$ ), which allows additional network sizes while maintaining the same routing principle.

**Routing algorithm.** The triangular layouts can be routed by the unified pair-removal recursion described in Sec. 4.5. Algorithm 1 gives a convenient stage-based formulation

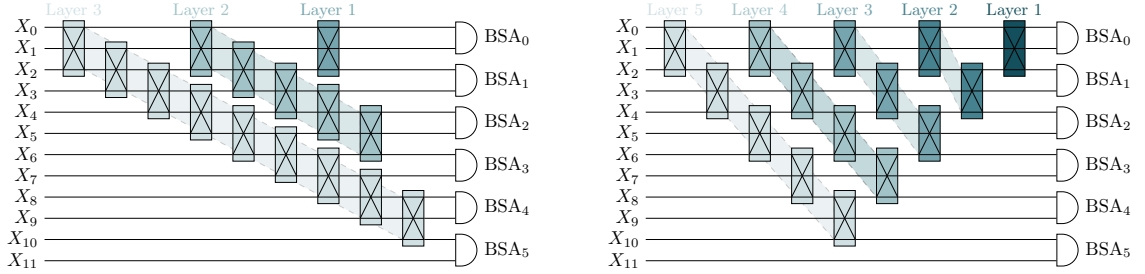
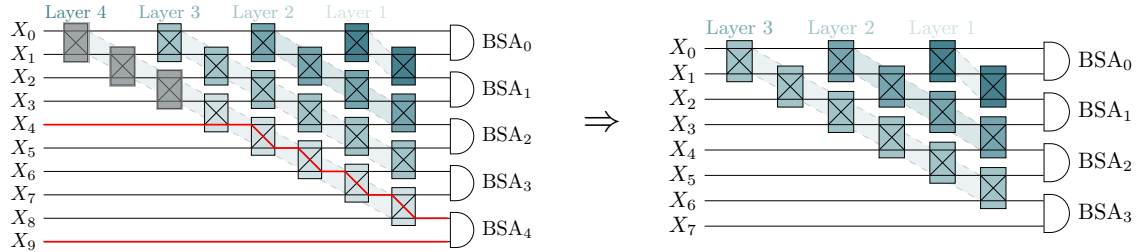


Figure 4.3: Two triangular  $3 \times 3$  fabrics for  $N = 12$  with different stage extraction capacities.

Left:  $q = 2$  pairs can be extracted per stage, consisting of three stages. Right:  $q = 1$  pair extracted per stage, consisting of five stages. Both realize the same planar non-blocking pair-to-BSA functionality with the minimal total number of switching elements.

for the triangular geometry, by fixing the non used switches in layer to BAR and creating a smaller triangular instance.



**2 × 2 triangular routing.** Setting  $M = 2$  gives  $M - 1 = 1$ , so each stage can extract at most one pair. Figure 4.4 shows the smallest nontrivial triangular instance with  $2 \times 2$  switches.

Choosing

$$q = 1 \quad \text{for all stages } s \tag{4.10}$$

reduces Algorithm 1 to the  $2 \times 2$  triangular routing specified in [25]. Each diagonal layer extracts exactly one pair ( $q = 1$ ) from the bottom boundary and forwards it to a BSA port. After removing the resolved pair, the remaining switch-point pattern is itself a triangular fabric on  $n - 2$  channels. Algorithm 2 is exactly Algorithm 1 under this specialization.

## (2) Pizza slice layout

The pizza slice layout is closely related to the triangular layout in that both are obtained by repeatedly wrapping a smaller fabric with an outer boundary chain and then using that boundary to extract pairs. The difference is how the fabric grows when increasing  $N$ . In the pizza slice layout, each expansion adds one new channel at the top and one at the

---

**Algorithm 1** Routing for triangular  $M \times M$  fabrics with constant per-layer extraction capacity  $q \in [1, M - 1]$

---

**Input:**  $Photons = (X_0, \dots, X_{N-1})$  (ordered top-to-bottom),  
 $PL$  : set of disjoint pairs  $\{(X_a, X_b)\}$ ,  
 $M$  : switch radix,  
 $q$  : extracted pairs per layer ( $1 \leq q \leq M-1$ ).  
**Output:** Switch configurations  $\{SW_k^s\}$  for all switches and stages.

```

1: procedure ROUTE_TRIANGLE_MxM( $Photons, PL, M, q$ )
2:    $SW \leftarrow \emptyset$ 
3:    $b \leftarrow 0$                                  $\triangleright$  next free BSA index; occupies boundary slots  $(2b, 2b+1)$ 
4:    $s \leftarrow 0$ 
5:   while  $|PL| > 0$  do
6:      $Q \leftarrow \min(q, |PL|, M - 1)$ 
7:      $P_s \leftarrow \text{SELECTPAIRS}(Photons, PL, Q)$        $\triangleright$  choose  $Q$  disjoint pairs to extract
8:      $T_s \leftarrow \{(2b, 2b+1), (2(b+1), 2(b+1)+1), \dots, (2(b+Q-1), 2(b+Q-1)+1)\}$        $\triangleright Q$ 
       target adjacent slots
9:      $SW_*^s \leftarrow \text{CONFIGURESTAGE}(Photons, P_s, T_s, M, s)$ 
10:     $SW \leftarrow SW \cup SW_*^s$ 
11:     $Photons \leftarrow \text{APPLYSTAGE}(Photons, SW_*^s, s)$ 
12:     $PL \leftarrow PL \setminus P_s$ 
13:     $b \leftarrow b + Q$ 
14:    if  $|PL| = 0$  then
15:      break
16:     $s \leftarrow s + 1$ 
17:  return  $SW$ 

```

---

bottom of the existing instance, and extends the outermost boundary chain accordingly. This symmetric growth provides a symmetric set of switch interactions for routing photons toward the bottom-most wire  $X_{N-1}$ . By contrast, the triangular layout grows only on one side where, each expansion appends two new channels at the bottom and adds a new boundary chain there.

**Recursion invariant.** Let the current unresolved size be  $n$  (initially  $n = N$ ). Choose  $q \leq M - 1$  disjoint pairs to extract. Configure the outermost band of the pizza slice so that these  $q$  pairs occupy  $q$  disjoint adjacent slot pairs at the boundary. After forwarding them to BSAs, remove the committed band and the  $2q$  resolved photons. The residual pattern can be redrawn as the same pizza slice layout on  $n - 2q$  channels (up to relabeling and a constant number of boundary elements fixed to BAR). This establishes a shape-preserving recursion and an inductive rearrangeable non-blocking proof.

**Recursive routing algorithm.** The pizza slice layout uses the same pair-removal recursion as the other designs (Algorithm 6); Algorithm 3 is a pizza slice-specific presentation of the same idea, where the available switch interactions are those of the pizza slice boundary band. Figure 4.6 illustrates the pizza slice layout instantiated with  $2 \times 2$  switches.

---

**Algorithm 2** Triangular  $2 \times 2$  routing in the stage-capacity template ( $M = 2, q = 1$ )

---

**Input:**  $\text{Photons} = (X_0, \dots, X_{N-1})$ , pairing set  $PL$ .  
**Output:** switch states  $\{SW_j^l\}$  (Bar/Cross).

```

1: procedure ROUTE_TRIANGLE_2x2( $\text{Photons}, PL$ )
2:    $SW \leftarrow \emptyset$ 
3:    $n \leftarrow |\text{Photons}|$ 
4:   while  $n > 2$  do                                 $\triangleright$  Stage  $s$  of Algorithm 1 with  $M=2$  and  $Q=1$ 
5:      $bot \leftarrow \text{Photons}[n - 1]$ 
6:      $p \leftarrow \text{partner of } bot \text{ in } PL$ 
7:      $i \leftarrow \text{index of } p \text{ in } \text{Photons}$            $\triangleright 0 \leq i \leq n - 2$ 
9:     Set switch layer  $l \leftarrow n/2 - 1$ 
10:     $SW \leftarrow SW \cup \{SW_j^l = \text{Bar} \mid 0 \leq j < i\}$ 
11:     $SW \leftarrow SW \cup \{SW_j^l = \text{Cross} \mid i \leq j \leq n - 3\}$        $\triangleright$  Target slots  $T_s$  are the last adjacent pair  $(n - 2, n - 1)$ 
12:     $\text{Photons} \leftarrow \text{move } \text{Photons}[i] \text{ to position } n - 2$        $\triangleright$  Extract one pair and recurse on the remaining photons
13:     $PL \leftarrow PL - \{(p, bot)\}$ 
14:     $n \leftarrow n - 2$ 
15:   return  $SW$ 

```

---

As in the triangular case, one pair is extracted per recursive step. After removing the outer boundary band and the resolved pair, the remaining unused fabric can be redrawn as a smaller pizza slice instance on  $n - 2$  channels, preserving the recursion invariant.

### (3) Chevron layout

The chevron layout has a more symmetric planar reduction construction. Intuitively, instead of extracting pairs from one edge, the chevron routes selected pairs to meet near the center and then forwards those adjacent outputs to the BSA pool. This symmetry is attractive for photonic implementations because it tends to reduce systematic depth

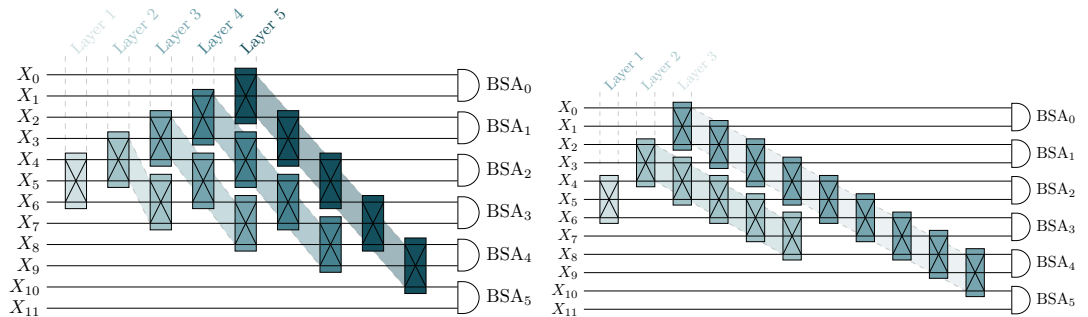


Figure 4.5: Two pizza slice  $3 \times 3$  fabrics for  $N = 12$

- . The pizza slice routes selected pairs to become adjacent near the center before forwarding them to the BSA pool.

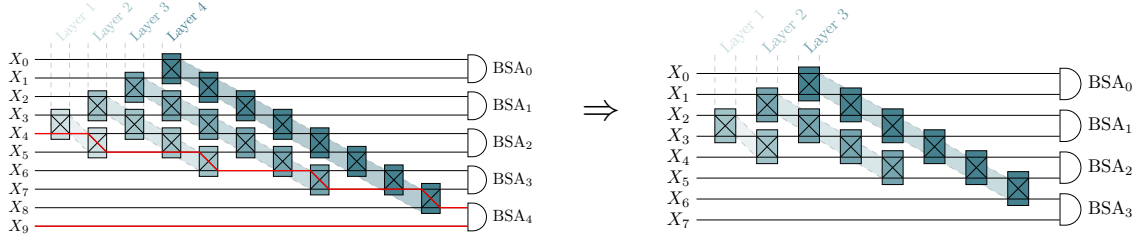


Figure 4.6: Recursive example for pizza slice  $2 \times 2$  fabrics for  $N = 10$   
 Left: initial unresolved pattern with 10 channels.  
 Right: after extracting one pair at the bottom boundary, and removing the switches in the layer, the remaining unresolved pattern is itself a pizza slice fabric on 8 channels.

imbalance between the top and bottom halves of the inputs.

**Stage capacity and recursion.** In one chevron step, we can extract between  $Q = 1$  and  $Q = M - 1$  pairs to adjacent output ports near the center seam.

The chevron pattern is shape-preserving under pair removal. After configuring the current chevron band so that  $Q \leq M - 1$  selected pairs become adjacent at the center and are forwarded to BSAs, removing the committed band and the  $2Q$  resolved photons leaves a residual pattern that can be redrawn as a smaller chevron instance on  $n - 2Q$  channels.

There are  $(M - 1)$  chevron variants corresponding to a vertical offset of where the center-adjacent extraction slots are placed (the extraction capacity is controlled by  $q$ , not by the variant).

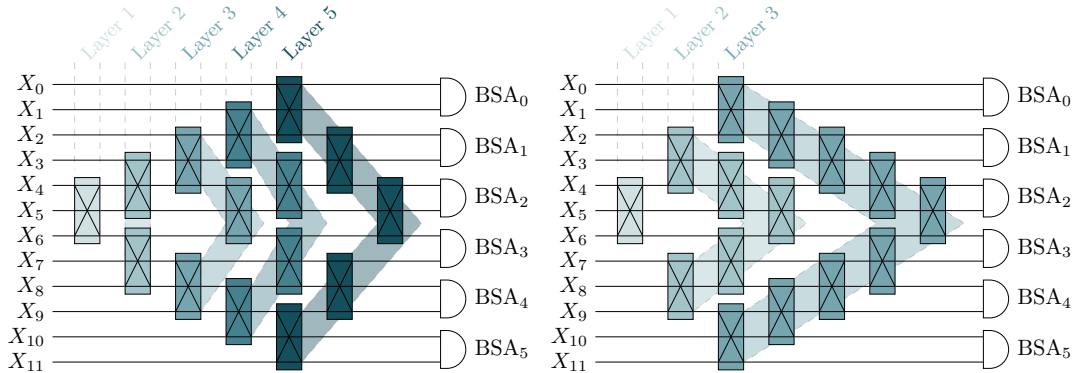


Figure 4.7: Two chevron  $3 \times 3$  fabrics for  $N = 12$   
 The chevron routes selected pairs to become adjacent near the center before forwarding them to the BSA pool.

**Chevron routing with  $M \times M$  switches.** Routing for chevron also follows the same pair-removal recursion: repeatedly take the bottom-most unresolved photon, push its partner toward the center seam using the earliest available switch interactions, and if needed push the bottom-most photon from the opposite side so that the pair becomes adjacent at the seam. After extracting  $q$  pairs, remove them and recurse on the smaller chevron instance.

---

**Algorithm 3** Recursive pizza slice routing for  $M \times M$  fabrics (boundary removal) with capacity  $q \in [1, M - 1]$

---

**Input:**  $Photons = (X_0, \dots, X_{n-1})$  (ordered top-to-bottom),  
 $PL$  : set of disjoint pairs  $\{(X_a, X_b)\}$ ,  
 $M$  : switch radix,  
 $q$  : extracted pairs per recursive step ( $1 \leq q \leq M - 1$ ).  
**Output:** switch configurations  $\{SW_k^s\}$ .

```

1: procedure ROUTE_TRIANGLE_RECURSIVE_MxM( $Photons, PL, M, q$ )
2:   if  $|Photons| \leq 2$  or  $|PL| = 0$  then
3:     return  $\emptyset$ 
4:    $n \leftarrow |Photons|$ 
5:    $s \leftarrow 0, SW \leftarrow \emptyset$ 
6:   while  $n > 2$  and  $|PL| > 0$  do
7:      $Q \leftarrow \min(q, |PL|, M - 1)$ 
8:      $P_s \leftarrow \text{SELECTPAIRS}(Photons, PL, Q)$ 
9:      $SW_*^s \leftarrow \text{CONFIGURESTAGE}(Photons, P_s, Q, M, s)$      $\triangleright$  configure the boundary
       band to realize  $q$  adjacencies
10:     $Photons \leftarrow \text{APPLYSTAGE}(Photons, SW_*^s, s)$ 
11:     $PL \leftarrow PL \setminus P_s$ 
            $\triangleright$  Remove the resolved pairs and recurse on the smaller pizza slice instance
12:     $Photons \leftarrow \text{REMOVERESOLVED}(Photons, Q)$      $\triangleright$  removes  $2Q$  photons (i.e.,  $Q$ 
       pairs)
13:     $n \leftarrow |Photons|$ 
14:     $s \leftarrow s + 1$ 
15:   return  $SW$ 

```

---

Algorithm 4 gives a stage-based chevron router parameterized by the stage extraction capacities  $q \in \{1, \dots, M - 1\}$ .

**$2 \times 2$  chevron example.** Figure 4.8 shows the chevron layout specialized to  $2 \times 2$  switches. In each step, the selected pair is routed to become adjacent at the center seam, after which it is forwarded to the BSA pool and removed. The remaining switch-point pattern forms a smaller chevron instance on  $n - 2$  channels.

#### 4.5.3 Hybrid layout

The layouts presented so far (triangular, pizza slice, and chevron) are *pure* recursive families: when the network size increases, the added switching band is always of the same geometric type. In this section I introduce a new *hybrid* design group, in which the fabric grows by *mixing* these recursive bands across steps.

**Key idea: mix-and-reduce recursion.** A hybrid fabric is constructed by starting from a small base instance and then repeatedly increasing the size by adding switches that can be chosen from the triangular, pizza slice, or chevron templates. After routing a

---

**Algorithm 4** Routing for chevron  $M \times M$  fabrics with constant per-layer extraction capacity  $q \in [1, M - 1]$

---

**Input:**  $\text{Photons} = (X_0, \dots, X_{N-1})$  (ordered top-to-bottom),  
 $PL$  : set of disjoint pairs  $\{(X_a, X_b)\}$ ,  
 $M$  : switch radix,  
 $q$  : extracted pairs per stage ( $1 \leq q \leq M-1$ ).  
**Output:** Switch configurations  $\{SW_k^s\}$  for all switches and stages.

```

1: procedure ROUTE_CHEVRON_MxM( $\text{Photons}, PL, M, q$ )
2:    $SW \leftarrow \emptyset$ 
3:    $s \leftarrow 0$ 
4:   while  $|PL| > 0$  do
5:      $n \leftarrow |\text{Photons}|$ 
6:      $Q \leftarrow \min(q, |PL|, M - 1)$ 
7:      $P_s \leftarrow \text{SELECTPAIRS}(\text{Photons}, PL, Q)$        $\triangleright$  choose  $Q$  disjoint pairs to extract
8:      $T_s \leftarrow \text{CHEVRONTARGETSLOTS}(n, Q)$        $\triangleright$   $Q$  target adjacent slots around the
       center seam
9:      $SW_*^s \leftarrow \text{CONFIGURESTAGE}(\text{Photons}, P_s, T_s, M, s)$ 
10:     $SW \leftarrow SW \cup SW_*^s$ 
            $\triangleright$  Apply the stage permutation and remove the extracted signals
11:     $\text{Photons} \leftarrow \text{APPLYSTAGE}(\text{Photons}, SW_*^s, s)$ 
12:     $PL \leftarrow PL \setminus P_s$ 
13:     $\text{Photons} \leftarrow \text{REMOVERESOLVED}(\text{Photons}, Q)$        $\triangleright$  remove  $2Q$  photons
14:    if  $|PL| = 0$  then
15:      break
16:     $s \leftarrow s + 1$ 
17:  return  $SW$ 

```

---

batch of pairs in the newly added band and committing the corresponding switch settings, the used portion of the layers is removed. The remaining unused fabric can be redrawn as a smaller instance of the hybrid construction . Therefore, the *same pair-removal recursion* of Sec. 4.5 still applies: route  $Q$  pairs, remove the committed region, and recurse on the residual fabric.

**Hybrid view of brickwork** ( $2 \times 2$ ). This perspective also explains why the  $2 \times 2$  brickwork is especially depth-efficient [25]: it can be interpreted as a hybrid construction obtained by composing *chevron-like* reductions repeatedly (“chevron within chevron”), but redistributed into a regular staggered grid. In other words, brickwork is not a different routing principle; it is a geometric rearrangement of consecutive seam-centered (chevron-style) reductions.

**Motivation: reducing maximum depth.** Hybrid layouts are attractive for photonic implementations because they allow trading geometric regularity for improved depth balance and a smaller maximum depth. Intuitively, seam-centered extraction (chevron-style) avoids pushing photons all the way to a single outer boundary, which tends to reduce the

---

**Algorithm 5** Chevron target slots around the center

---

**Input:** current size  $n$ , extracted pairs  $Q$   
**Output:**  $T = \{(t_1, t_1+1), \dots, (t_Q, t_Q+1)\}$

```

1: procedure CHEVRONTARGETSLOTS( $n, Q$ )
2:    $m \leftarrow \lfloor n/2 \rfloor$   $\triangleright$  for even  $n$ , seam is between  $m - 1$  and  $m$ ; for odd  $n$ ,  $m$  is the center
   line
3:    $T \leftarrow \emptyset$ 
4:   for  $r = 0$  to  $Q - 1$  do
5:     if  $r$  is even then
6:        $t \leftarrow (m - 1) - r/2$ 
7:     else
8:        $t \leftarrow m + (r - 1)/2$ 
9:      $T \leftarrow T \cup \{(t, t + 1)\}$ 
10:   return  $T$ 

```

---

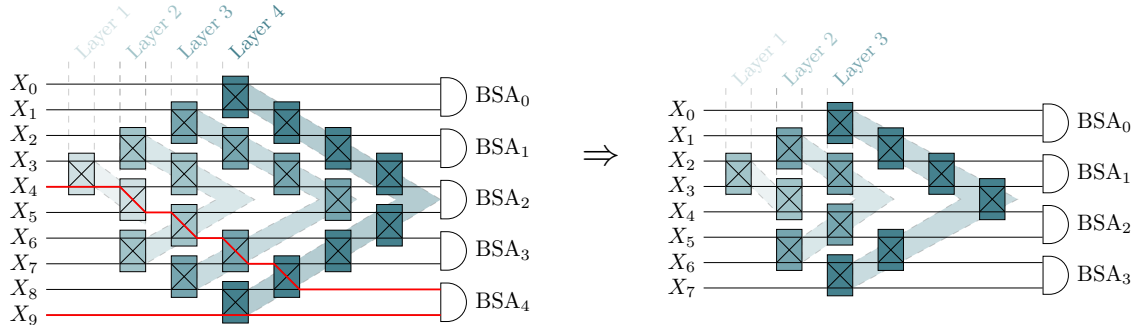
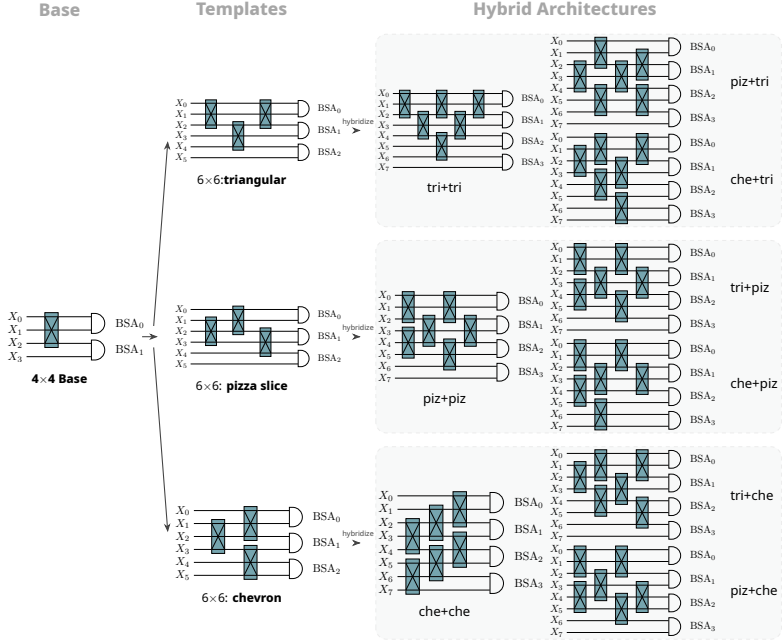


Figure 4.8: Recursive example for chevron  $2 \times 2$  fabrics for  $N = 10$   
Left: initial unresolved pattern with 10 channels.  
Right: after extracting one pair at the center seam, and removing the applicable switches, the remaining unresolved pattern is a chevron fabric on 8 channels.

depth imbalance between upper and lower inputs. For this reason, among the hybrid families, repeatedly composing chevron bands (chevron+chevron+...) is a natural candidate for a depth-minimizing design when  $M > 2$  as well. In this thesis I treat this as a design heuristic supported by the routing logic and by the observed depth patterns in constructed examples; a tight optimality proof over all planar layouts is left as future work.

**Construction procedure (general  $M$ ).** Fix a radix  $M$  and a base non-blocking instance (e.g., a small  $(N_0 \times N_0)$  fabric that is routable by the pair-removal recursion). To grow from size  $n$  to size  $n+2Q$ , choose a band type (triangular / pizza slice / chevron) that supports extracting  $Q \leq M - 1$  pairs in the next step. Place the band so that the unified routing step can make the selected  $Q$  pairs adjacent at the band output, forward them to the BSA pool, and commit the required switch states. After removing the committed band portion and the  $2Q$  resolved photons, the remaining unused fabric is isomorphic to the previous size- $n$  instance. Repeating this process yields a large hybrid fabric whose routing is constructive by recursion.



1

Figure 4.9: Hybrid-family construction examples for  $M = 3$ .

Left:  $4 \times 4$  base instance. Middle: three “pure”  $6 \times 6$  templates.

Right: representative  $8 \times 8$  hybrids obtained by adding one outer growth band whose type is chosen independently of the interior template. The filename convention encodes *interior*  $6 \times 6$  template (first three letters) + *outer band type* (last three letters).

Figure 4.9 summarizes the construction of the hybrid family for  $M = 3$  used in this thesis. Starting from a  $4 \times 4$  base instance, we first form three “pure”  $6 \times 6$  layouts (triangular / pizza slice / chevron). An  $8 \times 8$  hybrid is then obtained by adding one additional outer band whose *type* can be chosen independently of the  $6 \times 6$  interior. In the filenames, the first three letters denote the band type used for the outer  $8 \times 8$  growth (tri/piz/che), while the last three letters denote the  $6 \times 6$  interior template.

**Brickwork construction for  $2 \times 2$  switch points.** Figure 4.10 shows a  $2 \times 2$  brickwork instance with  $N = 10$ . For the  $2 \times 2$  case, a brickwork arrangement can be defined by the recursive optimal designs of [25]. This brickwork design is a set of combinations of smaller sizes of chevron-like reductions arranged in a staggered grid. An  $N \times N$  brickwork switch consists of  $N/2$  layers, each layer containing a set of disjoint adjacent  $2 \times 2$  switch points. Odd layers place switch points on the odd boundaries,

$$SW_1^k \rightarrow SW_3^k \rightarrow \cdots \rightarrow SW_{N-3}^k \quad (k \text{ odd}), \quad (4.11)$$

while even layers place switch points on the even boundaries,

$$SW_0^k \rightarrow SW_2^k \rightarrow \cdots \rightarrow SW_{N-2}^k \quad (k \text{ even}). \quad (4.12)$$

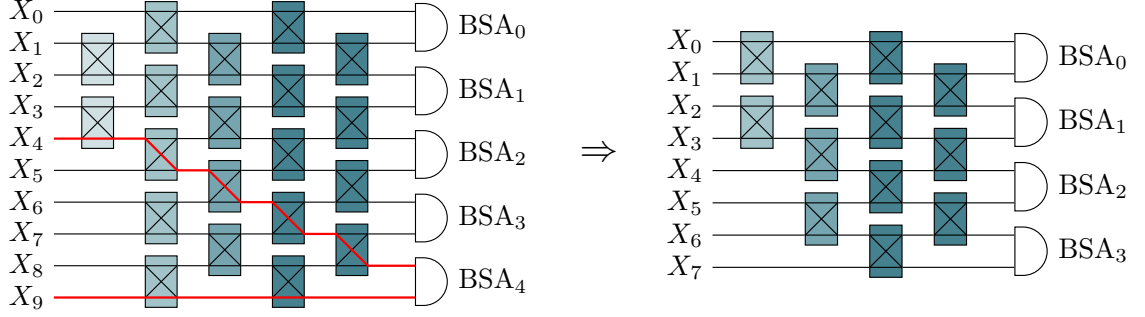


Figure 4.10: Recursive example for brickwork  $2 \times 2$  fabrics for  $N = 10$

Left: initial unresolved pattern with 10 channels.

Right: after extracting one pair at the center seam, and removing the applicable switches, the remaining unresolved pattern is a brickwork fabric on 8 channels.

This placement yields the same total number of switch points as the triangular and chevron layouts, namely  $N(N - 2)/4$  for  $M = 2$ .

## 4.6 Generalized Interconnect Fabrics

Beyond pair-to-BSA routing, some quantum interconnects require routing photons to intermediate switching nodes or to multiple processing modules. This motivates a generalized endpoint-routing design in which not all paths terminate at BSAs. I have preliminary switch-count bounds for this generalized setting; however, because additional verification is ongoing, I defer the full statement and proof to future work.

---

**Algorithm 6** Brickwork routing ( $2 \times 2$ ): path-removal recursion

---

**Input:** ordered photons  $Photons = (X_0, \dots, X_{N-1})$ , pair list  $PL$ .  
**Output:** switch states  $\{SW_j^k \in \{\text{Bar}, \text{Cross}\}\}$ .

- 1: **procedure** ROUTE\_BRICKWORK\_2x2( $Photons, PL$ )
- 2:   **if**  $|Photons| = 2$  **then**
- 3:     **return**  $\emptyset$
- 4:     $n \leftarrow |Photons|$ ,  $bot \leftarrow Photons[n - 1]$ ,  $p \leftarrow$  partner of  $bot$  in  $PL$
- 5:     $i \leftarrow$  index of  $p$  in  $Photons$   
            ▷ Create a monotone diagonal path: move  $p$  down as early as possible
- 6:    Commit switch states along the earliest-encounter diagonal that shifts  $p$  downward
- 7:    Let  $(j, j+1)$  be the adjacent meeting lines reached by this path
- 8:    **if**  $j \neq n - 2$  **then**    ▷ If  $p$  cannot reach  $n - 2$ , move  $bot$  up as late as possible to  
            meet at  $(j, j+1)$
- 9:       Commit switch states along a latest-encounter diagonal that shifts  $bot$  upward  
            to  $j+1$
- 10:      Set all other (unused) switch points in the affected layers to Bar
- 11:      Remove the committed paths and the resolved pair from  $(Photons, PL)$               ▷  
            Residual fabric is a brickwork of size  $n - 2$  (up to constant BAR fixes)
- 12:      **return** committed states  $\cup$  ROUTE\_BRICKWORK\_2x2( $Photons', PL'$ )

---

# Chapter 5

# Chip Specification

## 5.1 Purpose and scope

As stated in the previous chapters, a scalable  $N \times N$  optical switch can be constructed by interconnecting smaller switching elements. In order to realize a large port count switch suitable in use for quantum network, this thesis focuses on the design and simulation of a fundamental  $2 \times 2$  switch cells.

The  $2 \times 2$  switch has two input ports and two output ports, and its function to route an optical signal to the desired output is demonstrated by controlling the relative phase between two interferometer arms as shown in Fig. 5.1. In particular, the switch must support two states: *BAR*, where the signal exits from the corresponding output port, and *CROSS*, the signal is routed to the opposite output port. Throughout this thesis, the switching behavior is implemented using a Mach Zehnder Interferometer (MZI) architecture, where a phase shift  $\Delta\phi$  applied to one arm changes the interference condition at the second coupler, resulting BAR/CROSS routing. The primary performance objective is to minimize the loss while maintaining sufficient isolation between the desired and undesired outputs. This is important in quantum networking, since optical loss directly reduces the probability of successful photon transmission and thus lowers entanglement generation rate throughout the network. Thus the design workflow in Chapter 6 prioritizes low-loss waveguides, low-excess-loss couplers, and low-radiation-loss routing structures.

## 5.2 Platform Choices

This work targets a silica based integrated photonic platform using Ge-doped SiO<sub>2</sub> as the core material and SiO<sub>2</sub> as the cladding. The main motivation in using such materials is that silica based waveguides provide low propagation loss and stable guiding. Since both of the core and cladding are electrical insulators, carrier based modulation is not available, thus, in order to achieve switching, we use the thermo-optic effect that, where heating changes the effective refractive index and introduces a controllable phase shift.

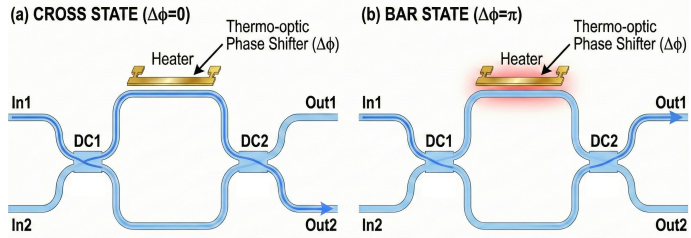


Figure 5.1: Operation principle of a Mach – Zehnder interferometer based  $2 \times 2$  switch. The device consists of two 50:50 directional couplers connected by two interferometer arms, one of which includes a controllable phase shifter. When the applied phase shift is  $\Delta\phi = 0$ , constructive interference directs the optical signal to the corresponding output port (BAR state). When  $\Delta\phi = \pi$ , the interference condition is inverted and the signal is routed to the opposite output port (CROSS state).

### 5.2.1 Wavelength

The target application of this chip is to interface the photonic switch with an ion-trap platform [10]. In  $^{88}\text{Sr}^+$ , a strong electric-dipole transition  $5s\,{}^2S_{1/2} \leftrightarrow 5p\,{}^2P_{1/2}$  occurs at  $\lambda \approx 421.7$  nm [26, 35]. When the ion is optically excited by a resonant (or near-resonant) 422 nm laser, it scatters fluorescence photons near 422 nm via spontaneous emission on this cycling transition (with additional repumping used in practice to avoid shelving in metastable  $D$  states) [14, 15]. For this reason, the switch is designed and simulated at an operating wavelength of 422 nm, and all component optimizations are performed to support efficient transmission at this wavelength.

### 5.2.2 Waveguide Platform

The waveguide consists of Ge-doped  $\text{SiO}_2$  core surrounded by  $\text{SiO}_2$  cladding. Silica based platforms have low loss routing, and are often used since they offer optical stability and relatively low absorption. In this thesis, the material dispersion is modeled (Chapter 6) to offer accurate effective index and phase estimates around the operating wavelength. Additionally, the waveguide geometry is chosen to support stable single-mode guiding under expected fabrication variations, and the final dimensions are selected from a region where both confinement and loss are robust.

### 5.2.3 Switching Mechanism

The  $2 \times 2$  switch is implemented using a thermo-optically tunable MZI. A resistive metal heater is placed above one interferometer arm, and electrical power is applied to increase the temperature. The temperature rise changes the refractive index through the thermo-optic coefficient, producing a phase shift  $\Delta\phi$  between the two arms. By tuning  $\Delta\phi$  to the temperature corresponding to constructive or destructive interference at the output coupler, the device transitions between BAR and CROSS states (Section 2.5.3 explains the general interferometric principle). Thermo-optic switching is slower than electro-optic switching since it is limited by thermal diffusion and device heat capacity. This platform

is expected to operate on about millisecond time scale.

### 5.3 Design Constraints

This section summarizes the constraints that bound the design. It is divided into two sections, *fabrication and geometry constraints*, which limit what can physically be realized, and *optical functional constraints*, which ensure that the fabricated device will behave as a interferometric switch.

#### 5.3.1 Fabrication and Geometry constraints

Although this thesis focuses on design and simulation, the design geometry is constrained by an assumed fabrication flow consisting of lithography, etching, cladding deposition, and metal heater formation. These steps impose practical limits on future size, alignment, and layer thickness. The switch is designed to be functional within the limits.

**Lithography resolution and minimum future size** Waveguide widths and coupling gaps are limited by the lithography tool and process accuracy. For the intended cleanroom environment, electro beam lithography (EBL) is assumed for pattern definition. As a conservative guideline, the minimum printable size of a waveguide is in order of 100 nm. Thus the minimum waveguide width, waveguide gaps in coupling regions, and the minimum heater line widths is defined.

**Etch and dimension control** The waveguide height is determined by the deposited core thickness and etch depth. However, the availability of Ge-doped SiO<sub>2</sub> deposition in the cleanroom is limited, and the final core thickness may depend on commercial deposition capabilities. For this reason, the design emphasizes on operating regions that are not highly sensitive to small changes in thickness, and assumed thickness can be refined once the deposition specifications are fixed.

**Cladding thickness and heater spacing** The upper cladding thickness affects both optical confinement, to reduce surface scattering, leakage, and thermal isolation, which effects the heater efficiency and crosstalk. The distance between the heater and core is limited by available cladding thickness. Placing the heater too close to the core will increase optical absorption and scattering, while placing it too far increases the required power for a  $\pi$  phase shift. In the baseline design, the cladding thickness is limited as a bounded parameter of  $\sim 1 \mu\text{m}$  as an initial practical limit.

#### 5.3.2 Optical functional constraints

**Single mode guiding** To avoid multi mode interference, the waveguide should operate in a single mode regime at  $\lambda = 422 \text{ nm}$ . In this thesis, the waveguide cross section is selected such that the higher order modes are suppressed and the device operation is dominated by the fundamental guided mode. This is important for quantum photonics,

since mixing modes can reduce interference visibility and introduce decoherence in encoded states.

**Interferometric compatibility and symmetry** The MZI switch relies on stable interference, therefore the two interferometer arms should be designed to be symmetric in geometry and length, except to the phase shifting region. Symmetry will reduce uncontrolled phase shift and balance loss between paths. This can improve the extinction ration and making the BAR and CROSS operating phase points the same.

**Directional coupler requirements** Directional couplers are used as the splitting and combining signals in the MZI. They should provide a 50/50 splitting ratio with minimal loss and unintended coupling outside of the designed coupler region. The coupling length will be shorter when the gap is smaller, but since fabrication variations may occur, the gap should be big enough to support it.

**Loss budget allocation** The total insertion loss arises for multiple components, including prorogation loss in straight sections, excess loss in coupler, and radiation loss in bends. To achieve low loss switch, each component must be optimized and validated in the full structure. Chapter 6 describes the step by step workflow to achieve low loss.

## 5.4 Design assumptions

To keep the design process tractable and to provide a clear baseline for future refinement, the following assumptions are adopted in this thesis:

**Operating wavelength:**  $\lambda = 422 \text{ nm}$ .

**Polarization:** targets the most guided mode, which is single TM-like polarization.

**Thermal operating range:** the device is assumed to operate in 300K with a heater induced temperature rise to achieve a  $\pi$  phase shift.

**Idealized fabrication:** baseline simulations assume ideal geometry without roughness or stochastic width variation.

Table 5.1: Design constraints and simulation status of the  $2 \times 2$  thermo-optic MZI switch.

Optical			
Category	Metric	Target / constraint	Current simulation
Optical	Operating wavelength	$\lambda = 422$ nm	$\lambda = 422$ nm
Optical	Modal operation	Single-mode operation	Fundamental guided mode used for evaluation ( $\text{TM}_0$ )
Optical	Insertion loss (IL)	As low as possible	CROSS: $ S_{14} ^2,  S_{23} ^2 \approx 0.83 \Rightarrow \text{IL} \approx 0.81$ dB; BAR: $ S_{13} ^2,  S_{24} ^2 \approx 0.82 \Rightarrow \text{IL} \approx 0.86$ dB
Optical	Extinction ratio (ER)	Suppress leakage	$\text{ER} \approx 10 \log_{10}(P_{\text{desired}}/P_{\text{leak}}) \sim 29\text{--}30$ dB (from $P_{\text{leak}} \sim 10^{-3}$ and $P_{\text{desired}} \sim 0.82$ )
Optical	Crosstalk leakage	Minimize undesired output power	Worst-case leakage $\sim 1 \times 10^{-3}$ (power), corresponding to $\sim -30$ dB crosstalk
Optical	Back-reflection	Low reflections	Not yet evaluated rigorously; very small in extracted power matrices (e.g., $ S_{11} ^2,  S_{22} ^2 \ll 10^{-8}$ )
Thermal / Fabrication / System			
Category	Metric	Target / constraint	Current simulation
Thermal	$\pi$ phase shift feasibility	Achieve $\pi$ phase shift	$\Delta n_\pi = \lambda/(2L) \approx 2.64 \times 10^{-4}$
Thermal	Heater power	Within practical budget	$\sim 8$ W for $\Delta T \sim 25$ K
Thermal	Thermal crosstalk	Neighbor phase error below tolerance	Not yet quantified
Layout	Minimum coupling gap	$\geq 200$ nm (EBL assumption)	selected coupling gap $g = 0.77 \mu\text{m}$ for robust 50/50 split
Layout	Bend / s-bend geometry	Avoid radiation loss	s-bend sweep: 20–200 $\mu\text{m}$ ; selected $L_s = 80 \mu\text{m}$ with $\sim 0.01$ dB insertion loss (near-adiabatic)
Layout	Footprint per cell	Must scale	1880 $\mu\text{m}$ in propagation axis

# Chapter 6

## Simulation Methodology

This chapter describes the simulation workflow used to design a low-loss  $2 \times 2$  optical switch using Ge-doped SiO<sub>2</sub> waveguides. The switch is decomposed into fundamental components, and each component is simulated using Ansys Lumerical MODE (FDE, EME) and the HEAT solver. The results are then combined to determine the device geometry and operating conditions.

### 6.1 Overview of Simulation Workflow

To obtain the final switch design, the fundamental parts of the switch are designed and then integrated into a complete device.

1. Define wavelength dependent material models using Sellmeier equation
2. Determine waveguide dimensions that support only fundamental modes
3. Design the directional coupler by sweeping the coupling gap and coupling length
4. Design the non-coupling region to suppress interaction between the waveguides
5. Connect the coupling and non-coupling region using a low-loss s-bends
6. Build a Mach Zehnder Interferometer(MZI) using two directional couplers
7. Add a thermo optic heater to enable phase shifting and switching between BAR and CROSS state

Each component is optimized individually and then integrated into a complete switch.

### 6.2 Numerical Solvers

Lumerical MODE provides three numerical solvers that are used throughout the design.

### 6.2.1 Finite Difference Eigenmode(FDE)

The FDE solver computes guided mode profiles by solving an eigenvalue problem derived from Maxwell's equations for the waveguide cross section. It returns the effective index  $n_{\text{eff}}$ , propagation loss, and the modal field fraction [3, 44].

### 6.2.2 Bidirectional Eigenmode Expansion(EME)

The EME solver propagates a modal decomposition of the electromagnetic field through long devices with longitudinally varying structures. By decomposing the geometry into a sequence of cells and solving for the supported modes in each cell, EME tracks modal evolution and coupling along the propagation direction. This approach is well suited to components such as coupling regions, S-bends, and full interferometers [5].

### 6.2.3 Heat Transport(HEAT)

The HEAT solver evaluates temperature rise under applied electrical power by solving the steady-state heat equation,

$$\nabla \cdot (k \nabla T) + Q = 0,$$

where  $T$  is temperature,  $k$  is the thermal conductivity, and  $Q$  is the volumetric heat generation rate. Using this solver, thermo-optic phase shifts can be derived [4].

## 6.3 Material Definition

The waveguide core is composed of Ge-doped SiO<sub>2</sub>, and the cladding is SiO<sub>2</sub>. Both of the materials have wavelength dependent refractive indices, thus the materials in Ansys are defined using Sellmeier equation taken from literature. This definition method provides accurate dispersion across small wavelength drifts around the operating wavelength of 422nm.

### 6.3.1 Waveguide Dimension Design

The dimension of the waveguide determines the number of supported optical modes. For too small dimensions, the waveguide becomes unguided, and for too large dimensions, higher-order modes appear. Higher-order modes will lead to interference between the modes, which can reduce the overall fidelity of the switch. Therefore, the design goal is to support only the fundamental modes.

To determine the appropriate dimensions, the core width and height were swept from 0.8 μm to 1.4 μm, and the number of modes found, effective index  $n_{\text{eff}}$ , and propagation loss were recorded.

The following script was used for the sweep.

Listing 6.1: Lumerical script for waveguide dimension sweep.

```
wg_name      = "core";
num_modes    = 4;
```

```

width_values = linspace(0.8e-6, 1.4e-6, 7);
height_values = linspace(0.8e-6, 1.4e-6, 7);

Nx = length(width_values);
Ny = length(height_values);

neff_results = matrix(Nx, Ny, num_modes) * 0/0;
loss_results = matrix(Nx, Ny, num_modes) * 0/0;

for (i = 1:Nx) {
    for (j = 1:Ny) {

        width = width_values(i);
        height = height_values(j);

        switchtolayout;
        setnamed(wg_name, "x span", width);
        setnamed(wg_name, "y span", height);

        nm = findmodes;

        for (m = 1:num_modes) {
            if (m <= nm) {
                mode_name = "mode" + num2str(m);
                neff_results(i,j,m) = getdata(mode_name, "neff")(1);
                loss_results(i,j,m) = getdata(mode_name, "loss")(1);
            }
        }
    }
}

```

After filtering out geometries that support more than one mode, a region of low-loss was observed around  $1.0 \times 1.0 - 1.3 \times 1.3 \mu\text{m}$  as shown in Fig.6.1. I choose the waveguide dimension of  $1.2 \times 1.2 \mu\text{m}$ , which lies in the center of the stable region and provides robustness against fabrication variability. The simulations focus on the fundamental TM mode, which is well confined in the chosen waveguide geometry.

### 6.3.2 Directional Coupler Design

The directional coupler is the fundamental building block of the Mach–Zehnder interferometer (MZI) switch and serves as the elementary routing primitive throughout this thesis. Although the simulations in this chapter focus on a  $2 \times 2$  switch, the same directional coupler geometry is reused as a modular element in larger  $3 \times 3$  and general  $M \times M$  switch architectures.

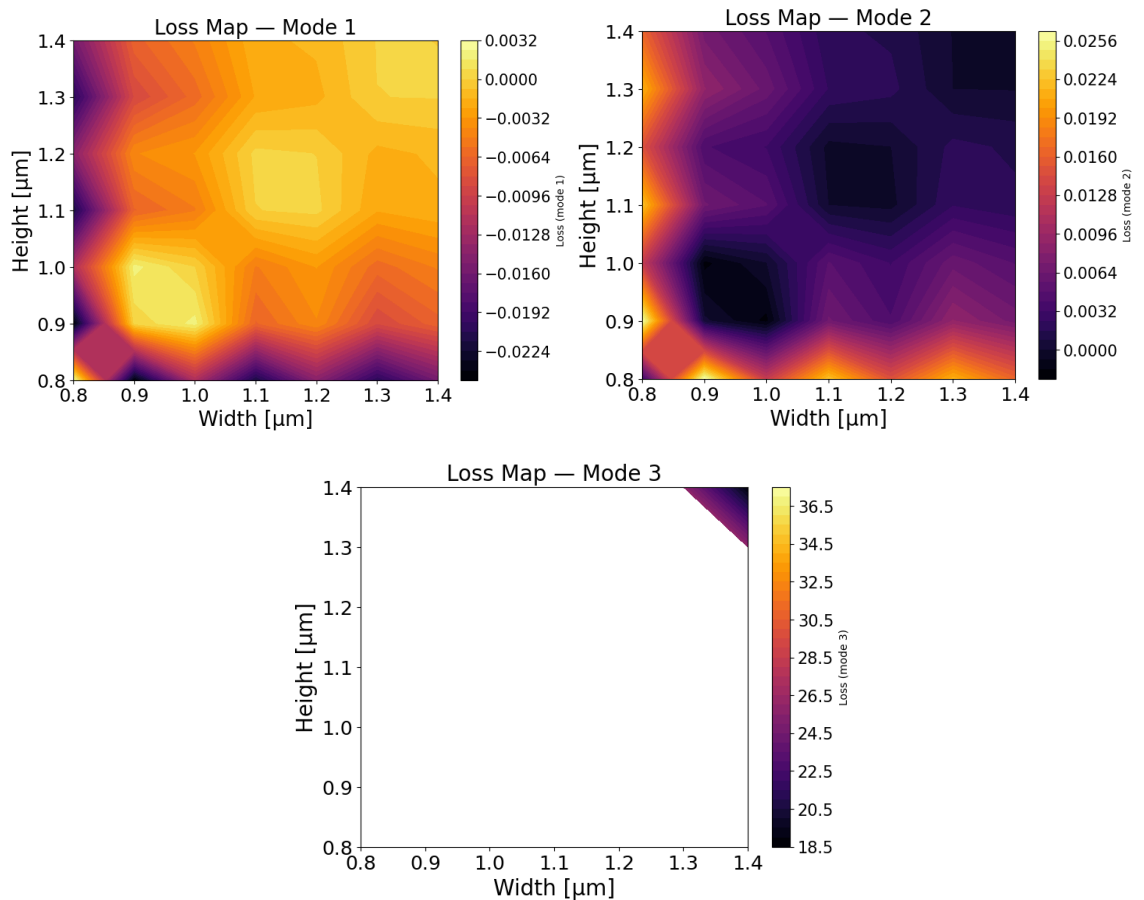


Figure 6.1: Propagation loss versus waveguide dimensions for the first three supported modes.

The x-axis represents the core width and the y-axis represents the core height. Mode 1 and Mode 2 are the fundamental modes, and blank regions indicate that the corresponding mode is not supported.

A directional coupler operates by bringing two identical waveguides into close proximity, allowing evanescent coupling between their guided modes. Optical power is exchanged periodically along the propagation direction, and by selecting an appropriate coupling gap and interaction length, a 50/50 power splitting condition can be achieved. This balanced splitting is required to ensure correct interference behavior in MZI-based switching networks.

To identify suitable design parameters, a two-dimensional parameter sweep was performed using the EME solver. The waveguide separation (coupling gap) was swept from  $0.6\text{ }\mu\text{m}$  to  $1.0\text{ }\mu\text{m}$ , and for each gap the coupling length was swept from  $125\text{ }\mu\text{m}$  to  $325\text{ }\mu\text{m}$ . For each parameter pair, the optical power at the bar and cross output ports was extracted to determine the coupling ratio.

Figure 6.2 (left) shows the coupling ratio as a function of gap and coupling length. The regions where the coupling ratio approaches 0.5 correspond to 50/50 splitting. As expected, the required coupling length increases with increasing gap due to reduced evanescent field overlap. For smaller gaps, multiple coupling periods are observed, resulting in additional 50/50 operating points at longer interaction lengths. In practice, the first coupling period is preferred to minimize device footprint and accumulated loss.

Based on these results, a coupling gap of  $0.77\text{ }\mu\text{m}$  was selected for the final design. This value provides a clear and well-isolated 50/50 operating point while maintaining robustness against fabrication variability. The corresponding coupling length is chosen from the first coupling period to reduce the physical size of each switching element. This consideration becomes increasingly important for  $3 \times 3$  and  $M \times M$  switch fabrics, where the total number of directional couplers scales with network size.

Figure 6.2 (right) shows the insertion loss (IL) extracted from the same sweep. The insertion loss is calculated by comparing the total output power to the input power. Around the selected gap of  $0.77\text{ }\mu\text{m}$ , the insertion loss is approximately  $0.47\text{--}0.52\text{ dB}$ . Analysis of the modal power distribution indicates that approximately 90% of the input power remains in the fundamental guided modes. Only 0.6% of the power is transferred to higher-order modes, corresponding to a fundamental mode purity of approximately 0.994. Maintaining high mode purity is particularly important for larger switch networks, where repeated mode leakage would otherwise accumulate and degrade overall performance.

It should be noted that the effective coupling length may be slightly shorter than the nominal straight coupling region length. This is because partial coupling can already occur within the S-bend transition region as the waveguides approach each other. As a result, the straight coupling section can be shortened in the final layout while still achieving the desired 50/50 splitting ratio. This effect is accounted for during full-device simulations of the MZI and becomes increasingly relevant when cascading many couplers in larger  $M \times M$  switch designs.

### 6.3.3 Non-Coupling Region

The non-coupling region sets a waveguide separation at which interaction between the two waveguides becomes negligible. An EME sweep of the separation distance was performed, and the cross-coupled power was extracted. Based on the results, a gap of  $2.4\text{ }\mu\text{m}$  was

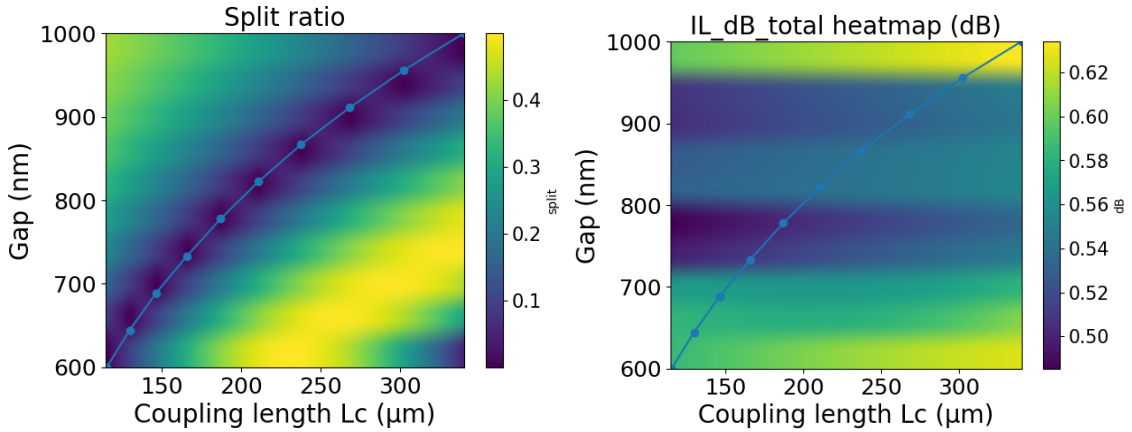


Figure 6.2: Simulated coupling ratio and insertion loss of the directional coupler. Left: Coupling ratio heatmap over coupling gap and coupling length. The blue line indicates the selected 50/50 operating point (gap and coupling length pair). Right: Insertion loss heatmap over coupling gap and coupling length. Around gap  $0.77\ \mu\text{m}$  the simulation shows low insertion loss.

selected as the non-coupling separation, where the cross-coupled power is below  $-60\ \text{dB}$ , indicating negligible interaction.

### 6.3.4 S-Bend Design

To smoothly transition between the coupling and non-coupling regions, an S-bend structure is introduced. The S-bend allows the waveguide separation to change adiabatically, minimizing radiation loss and mode conversion. This transition is necessary both within a single MZI and between adjacent switching elements in larger switch fabrics.

In the present design, the coupling gap is  $0.77\ \mu\text{m}$ , while the non-coupling gap is  $2.4\ \mu\text{m}$ . To symmetrically connect these regions, each waveguide must be displaced laterally by

$$\Delta x = \frac{2.4\ \mu\text{m} - 0.77\ \mu\text{m}}{2} = 0.81\ \mu\text{m}.$$

An S-bend is therefore used to introduce this lateral offset while preserving modal integrity.

The S-bend length was swept from  $20\ \mu\text{m}$  to  $200\ \mu\text{m}$  using the EME solver, and the bend loss was extracted by comparing the transmitted power at the output to the input power. Short S-bends introduce stronger curvature, leading to increased radiation loss and coupling to higher-order modes. Longer S-bends reduce curvature-induced loss but increase device footprint.

Figure 6.3 shows the simulated field profile and transmission behavior for the S-bend structure. From the sweep results, a bend length of  $80\ \mu\text{m}$  was selected. At this length, the simulated insertion loss is approximately  $0.01\ \text{dB}$ , indicating that the bend is sufficiently gentle to avoid significant mode conversion.

### 6.3.5 Mach Zehnder Interferometer(MZI)

Two directional couplers connected by two parallel waveguide arms form a Mach–Zehnder interferometer (MZI). By introducing a relative phase difference between the two arms,

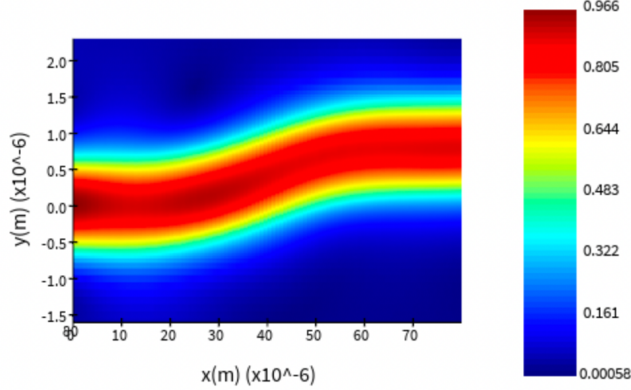


Figure 6.3: Simulation monitor for s-bend connecting coupling and non-coupling region. A field profile from the Ansys EME solver. High optical power (red) propagates through the S-bend with low loss. The bend length of  $80\mu\text{m}$  was selected for the final design.

the interference condition at the second directional coupler can be controlled, enabling switching between the BAR and CROSS states.

**Phase accumulation and switching condition** For a straight waveguide section of length  $L$ , the optical phase accumulated by the guided mode is given by

$$\phi = \frac{2\pi}{\lambda} n_{\text{eff}} L, \quad (6.1)$$

where  $\lambda$  is the operating wavelength and  $n_{\text{eff}}$  is the effective refractive index of the guided mode. A relative phase shift between the two arms of the MZI is therefore expressed as

$$\Delta\phi = \frac{2\pi}{\lambda} \Delta n_{\text{eff}} L, \quad (6.2)$$

where  $\Delta n_{\text{eff}}$  represents the effective index difference between the two arms over the interaction length  $L$ .

The MZI exhibits two characteristic operating points:

- *BAR state*:  $\Delta\phi = 0 \pmod{2\pi}$ , where the optical field exits from the corresponding output port.
- *CROSS state*:  $\Delta\phi = \pi$ , where the optical field is routed to the opposite output port.

Thus, a  $\pi$ -phase shift is the fundamental requirement for switching operation. From the above relation, the condition for achieving a  $\pi$ -phase shift is

$$\Delta n_{\text{eff}} L = \frac{\lambda}{2}. \quad (6.3)$$

In the present design, the operating wavelength is  $\lambda = 422\text{ nm}$  and the baseline effective index of the fundamental mode is  $n_{\text{eff}} = 1.48653$ . For an arm length of approximately  $800\mu\text{m}$ , the required effective index modulation is on the order of  $2.6 \times 10^{-4}$ . This value provides a useful reference for both numerical phase tuning and subsequent thermo-optic heater design.

**Scattering matrix formalism** The behavior of the MZI is quantitatively described using a scattering matrix (S-matrix) representation. In this formalism, the relationship between the complex input and output field amplitudes is written as

$$\mathbf{b} = \mathbf{S} \mathbf{a}, \quad (6.4)$$

where  $\mathbf{a}$  and  $\mathbf{b}$  denote the vectors of incoming and outgoing modal field amplitudes at the defined ports, respectively. Each matrix element  $S_{ij}$  represents the complex transmission coefficient from input port  $j$  to output port  $i$ , including both amplitude and phase information.

The optical power transmitted from port  $j$  to port  $i$  is obtained from the squared magnitude of the corresponding matrix element,  $|S_{ij}|^2$ . For an ideal lossless and fully monitored system, the S-matrix is unitary and satisfies power conservation. In practical numerical simulations, deviations from unitarity arise due to radiation loss, absorption, or coupling to modes not included in the monitored port set. Nevertheless, the S-matrix provides a compact and physically transparent description of routing efficiency, insertion loss, and crosstalk, and is therefore used throughout this thesis to evaluate switching performance.

In the simulations, the top input is defined as port 1, the bottom input as port 2, the top output as port 3, and the bottom output as port 4. Thus, the S-matrix of the MZI can be expressed as

$$\mathbf{S} = \begin{pmatrix} S_{11} & S_{12} & S_{13} & S_{14} \\ S_{21} & S_{22} & S_{23} & S_{24} \\ S_{31} & S_{32} & S_{33} & S_{34} \\ S_{41} & S_{42} & S_{43} & S_{44} \end{pmatrix}, \quad (6.5)$$

where  $S_{13}$  and  $S_{24}$  represent the BAR port transmissions, while  $S_{14}$  and  $S_{23}$  represent the CROSS port transmissions.

**Numerical implementation and S-matrix analysis** To verify the switching behavior, the full MZI structure was simulated using the EME solver by connecting the components simulated in the previous sections. A controlled phase difference was introduced between the two arms by locally modifying the refractive index of one arm, allowing direct evaluation of the interference response without invoking the thermal model.

The device performance was analyzed using the user-defined scattering matrix extracted from the EME simulation. Each matrix element  $S_{ij}$  represents the complex field transmission coefficient from input port  $j$  to output port  $i$ . The optical power transmission is obtained from the squared magnitude,  $|S_{ij}|^2$ .

For the CROSS-state configuration, the S-matrix exhibits dominant diagonal elements, indicating efficient routing to the opposite output port, while the off-diagonal elements remain several orders of magnitude smaller as shown in Eq. (6.6) and is illustrated in Fig. 6.4. The extracted power transmission is approximately  $|S_{ij}|^2 \approx 0.83$  in the fundamental guided mode. This corresponds to an insertion loss of  $-10 \log_{10}(0.83) \approx 0.81$  dB (within the monitored mode set). The remaining power is attributed to radiation loss and weak coupling to unmonitored modes. An example of the extracted CROSS-state power

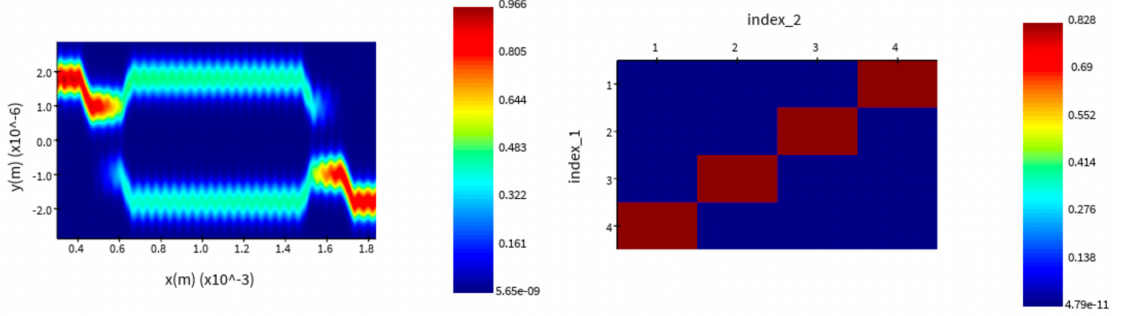


Figure 6.4: Simulation monitor and S-matrix of the MZI in CROSS state.  
Left: A field profile from the Ansys EME solver showing propagation through the MZI in the CROSS state. Right: S-matrix extracted from the EME simulation showing high transmission in the CROSS ports and low crosstalk in the BAR ports.

matrix is shown in Eq. (6.6).

$$|\mathbf{S}_{\text{CROSS}}|^2 \approx \begin{pmatrix} 6.3 \times 10^{-17} & 1.0 \times 10^{-8} & 2.22 \times 10^{-5} & 8.26 \times 10^{-1} \\ 1.0 \times 10^{-8} & 1.22 \times 10^{-14} & 8.26 \times 10^{-1} & 3.0 \times 10^{-5} \\ 1.58 \times 10^{-5} & 8.27 \times 10^{-1} & 1.1 \times 10^{-3} & 4.72 \times 10^{-10} \\ 8.27 \times 10^{-1} & 2.19 \times 10^{-5} & 3.82 \times 10^{-10} & 1.95 \times 10^{-13} \end{pmatrix}, \quad (6.6)$$

where the dominant CROSS-port field transmission corresponds to a power transmission of approximately  $|S_{ij}|^2 \approx 0.83$  in the monitored fundamental mode.

For the BAR-state configuration, the dominant power appears in the BAR-port elements ( $S_{13}$  and  $S_{24}$ ). To make the interpretation explicit, Eq. (6.7) reports the power matrix  $|S_{ij}|^2$  obtained from the EME monitor.

$$|\mathbf{S}_{\text{BAR}}|^2 \approx \begin{pmatrix} 2.34 \times 10^{-8} & 1.60 \times 10^{-10} & 8.16 \times 10^{-1} & 1.07 \times 10^{-3} \\ 8.08 \times 10^{-11} & 1.92 \times 10^{-8} & 9.72 \times 10^{-4} & 8.06 \times 10^{-1} \\ 8.18 \times 10^{-1} & 1.05 \times 10^{-3} & 2.39 \times 10^{-8} & 1.36 \times 10^{-10} \\ 9.96 \times 10^{-4} & 8.07 \times 10^{-1} & 8.11 \times 10^{-11} & 1.95 \times 10^{-8} \end{pmatrix}. \quad (6.7)$$

The measured BAR-port transmission is approximately 0.81–0.82 per input, corresponding to an insertion loss of  $-10 \log_{10}(0.82) \approx 0.86$  dB (within the monitored mode set). The strongest undesired terms are on the order of  $10^{-3}$ , corresponding to crosstalk of roughly –30 dB. The remaining  $\sim 18\%$  of the input power is attributed to radiation loss and coupling to modes not included in the monitored port set.

This S-matrix-based analysis confirms that the MZI operates as an effective  $2 \times 2$  switch with low crosstalk and well-defined BAR and CROSS states. The same analysis framework is later reused to evaluate larger  $3 \times 3$  and general  $M \times M$  switching fabrics, where accurate phase control and interference behavior remain essential.

### 6.3.6 Thermo-Optic Heater Design

A heater placed above one arm of the MZI enables switching by modifying the effective index through the thermo-optic effect. Using the HEAT solver, the steady-state temper-

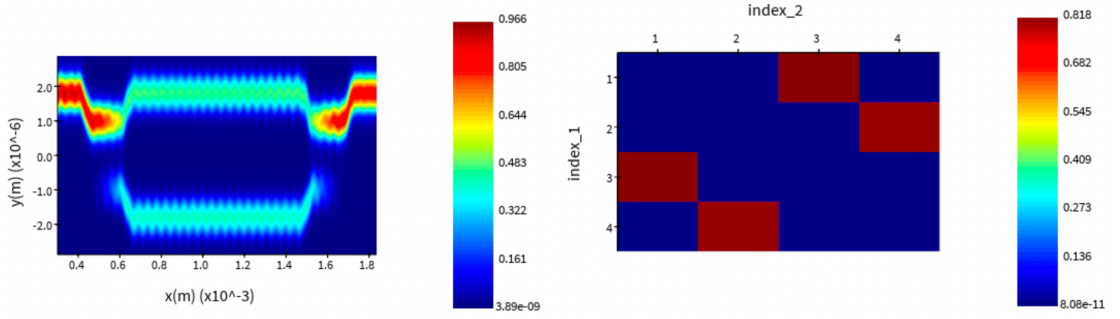


Figure 6.5: Simulation monitor and S-matrix of the MZI in BAR state. Left: A field profile from the Ansys EME solver showing propagation through the MZI in the BAR state. Right: S-matrix extracted from the EME simulation showing high transmission in the BAR ports and low crosstalk in the CROSS ports.

ature rise  $\Delta T(x, y)$  under applied electrical power is simulated and then mapped to an effective-index change  $\Delta n_{\text{eff}}$ . By computing the required  $\Delta n_{\text{eff}}$  for a  $\pi$  phase shift, the heater geometry and operating power can be selected.

**Required index shift from the switching condition** From Section 6, the phase shift accumulated over a heater (phase-shifter) length  $L$  is

$$\Delta\phi = \frac{2\pi}{\lambda} \Delta n_{\text{eff}} L. \quad (6.8)$$

To switch between BAR and CROSS states, the required condition is  $\Delta\phi = \pi$ , which yields

$$\Delta n_{\text{eff}} = \frac{\lambda}{2L}. \quad (6.9)$$

In the EME switching simulations, the phase-shifting arm effective index changes from

$$\text{CROSS (unheated): } n_{\text{phase}} = 1.48653, \quad (6.10)$$

$$\text{BAR (heated): } n_{\text{phase}} = 1.48685, \quad (6.11)$$

for a phase-shifter length of  $L = 800 \mu\text{m}$ . Thus, the required index change is

$$\Delta n_{\text{eff}} = 1.48685 - 1.48653 = 3.2 \times 10^{-4}. \quad (6.12)$$

**Converting  $\Delta n_{\text{eff}}$  to temperature rise** A first-order thermo-optic relation links refractive-index change to temperature rise:

$$\Delta n_{\text{eff}} \approx \Gamma \left( \frac{dn}{dT} \right) \Delta T, \quad (6.13)$$

where  $dn/dT$  is the thermo-optic coefficient of the waveguide core material and  $\Gamma$  is an effective overlap (confinement) factor that accounts for the fraction of the guided mode overlapping the heated region. For integrated waveguides,  $\Gamma$  typically lies in the range 0.7–0.9; in this thesis,  $\Gamma = 0.8$  is used as a representative value.

Using Eq. (6.13), the required temperature rise is

$$\Delta T \approx \frac{\Delta n_{\text{eff}}}{\Gamma (dn/dT)}. \quad (6.14)$$

As an example, taking  $(dn/dT) = 1.3 \times 10^{-5} \text{ K}^{-1}$  and  $\Gamma = 0.8$  gives

$$\Delta T \approx \frac{3.2 \times 10^{-4}}{0.8 \times 1.3 \times 10^{-5}} \approx 30.8 \text{ K}. \quad (6.15)$$

**Choice of thermo-optic coefficient** The thermo-optic coefficient depends on glass composition, fabrication conditions, and wavelength. For GeO<sub>2</sub>-doped silica glass fibers, Rego reports room-temperature values on the order of  $dn/dT \sim 8.5 \times 10^{-6} \text{ K}^{-1}$  for the Ge-doped core (SMF-28) and discusses higher values for bulk GeO<sub>2</sub> (e.g.,  $\sim 18 \times 10^{-6} \text{ K}^{-1}$  at  $1.55 \mu\text{m}$ ) [32]. Because this thesis operates at 422 nm and uses Ge-doped SiO<sub>2</sub> waveguides rather than fibers, the literature value is used as a physically grounded reference and the final heater power is determined from the HEAT-simulated  $\Delta T$  and the extracted  $\Delta n_{\text{eff}}$  for the specific device geometry.

## 6.4 Summary

Through a combination of FDE, EME, and HEAT simulations, I obtain a complete low-loss design for the  $2 \times 2$  photonic switch. The insertion loss for CROSS and BAR states are approximately 0.81 dB and 0.86 dB respectively, with crosstalk below  $-30$  dB. Waveguide dimensions, coupling behavior, bend geometry, interferometer structure, and thermo-optic phase shifting are optimized systematically, forming a functional switching element suitable for integration into larger quantum photonic circuits.

# Chapter 7

## Evaluation and Discussion

### 7.1 Scalability and Resource Analysis

A central objective of this work is to design an optical switching network that scales efficiently with the number of ports while remaining physically realizable on an integrated photonic platform. In this section, the scalability of the proposed architecture is evaluated in terms of switch count, network depth, and structural regularity, and is compared against naive and conventional switching approaches.

For an  $N \times N$  switching network constructed from  $M \times M$  switch elements, the proposed design exploits a recursive reduction strategy, as introduced in Chapter 4. At each stage of the routing process, a subset of input–output connections is deterministically assigned, reducing the effective problem size. This recursive structure directly impacts both the total number of switch elements required and the maximum number of switches traversed by a signal.

**Switch count scaling** In a naive crossbar architecture, the number of switching elements scales as  $\mathcal{O}(N^2)$ , which quickly becomes impractical for large  $N$  due to loss constraints. In contrast, the proposed architecture requires a total number of switch elements that scales subquadratically as  $\mathcal{O}(N^2/M^2)$ . For the special case of  $2 \times 2$  switches, the total number of elements follows the  $N(N - 2)/4$ , while for larger  $M \times M$  switches, the number of required elements is further reduced due to the increased fan-out of each switching operation. This reduction directly translates into lower footprint and fewer optical components on chip. Fig. 7.1 illustrates the comparative scaling of switch count for different switch sizes.

**Switch depth** The switch depth, defined as the maximum number of switch elements encountered along any input–output path, is a critical metric for photonic implementations, as it determines the accumulated insertion loss and phase error. For the proposed design, the depth scales approximately as  $\mathcal{O}(N/M)$ , reflecting the fact that each switching stage resolves up to  $M$  channels simultaneously. Compared to architectures composed exclusively of  $2 \times 2$  switches, increasing the switch size  $M$  allows a reduction in depth at the cost of increased complexity within each individual switch element.

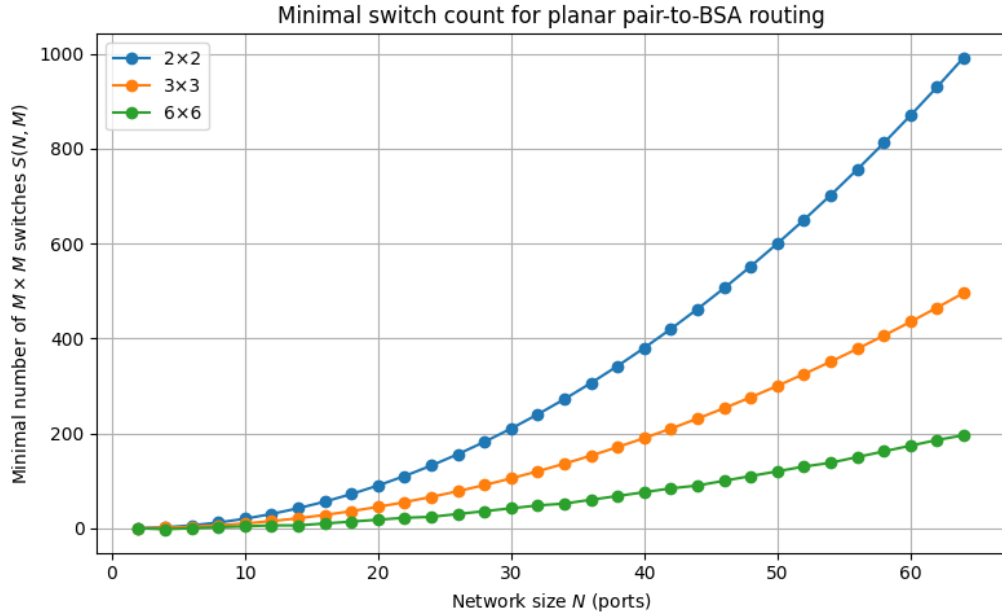


Figure 7.1: Comparison of switch count scaling for different architectures. The plot compares the total number of switch elements required for an  $N \times N$  switching network using  $2 \times 2$  switches (blue),  $3 \times 3$  switches (orange), and the  $6 \times 6$  switches (green). The proposed design demonstrates significantly improved scaling, particularly for larger switch sizes.

**Structural regularity** An additional advantage of the proposed design lies in its structural regularity. The recursive construction leads to repeated and symmetric switch layouts, which are well suited for photonic integrated circuit fabrication. Regular layouts simplify mask design, improve fabrication yield, and facilitate automated control and calibration procedures.

Overall, this scalability analysis demonstrates that the proposed switching architecture achieves a favorable trade-off between hardware resources and depth. By selecting an appropriate switch size  $M$ , the architecture can be adapted to different system requirements, balancing physical constraints such as loss and footprint against routing flexibility and control complexity. These properties make the design particularly attractive for large-scale quantum photonic networks, where scalability and loss management are paramount.

## 7.2 Expected Physical Performance

This section discusses the expected physical performance of the proposed switching elements based on electromagnetic simulations, with a focus on insertion loss, crosstalk behavior, and scalability trends.

### 7.2.1 Preliminary switching behavior

Electromagnetic simulations were performed for a single switching element operating in the fundamental transverse magnetic (TM) mode. Under these conditions, the CROSS state exhibits a normalized output power of approximately 0.83, corresponding to an insertion

loss of about 0.8 dB (computed as  $IL = -10 \log_{10}(0.83)$ ). Crosstalk to undesired output ports is observed to be minimal, suggesting that mode confinement and routing fidelity are well preserved in this configuration. From the simulated scattering matrix of the CROSS state, the worst-case crosstalk (maximum undesired output power relative to the desired output) is approximately  $-44.5$  dB.

The BAR-state performance is evaluated using the same metrics as the CROSS state. From preliminary BAR-state simulations, the normalized output power is approximately 0.82, corresponding to an insertion loss of about 0.86 dB. Crosstalk to undesired output ports is on the order of  $-30$  dB, consistent with the BAR-state scattering-matrix analysis presented in Chapter 6. These results indicate that the BAR state exhibits slightly higher loss than the CROSS state, while maintaining acceptable isolation between output ports.

### 7.2.2 Vertical cascading and loss accumulation

To evaluate scalability, it is instructive to consider how insertion loss accumulates as multiple switching elements are cascaded vertically along a single optical path. Given the observed CROSS state transmission of approximately 0.83, repeated traversal through identical switching stages will lead to an exponential decay in optical power, as illustrated in Fig. 7.2. In the following analysis, the CROSS state insertion loss is used as a representative per-switch loss value. This behavior suggests the existence of a practical upper bound on the number of cascaded switches that can be tolerated before the signal power falls below a usable baseline.

Assuming identical loss characteristics for each switching stage, the transmitted power after  $k$  cascaded switches can be approximated as

$$P_k \approx P_0 \cdot T^k, \quad (7.1)$$

Equivalently, in logarithmic units, the accumulated insertion loss after  $k$  cascaded switches can be approximated as  $IL_k \approx k \cdot IL_1$ , where  $IL_1$  denotes the single-switch insertion loss expressed in decibels and  $T$  is the single-switch transmission coefficient. Under the present simulation conditions, this implies that only a limited number of vertical switching layers can be accommodated before excessive attenuation occurs. This observation motivates the architectural emphasis on reducing network depth through larger switch elements and recursive routing strategies, as discussed in previous sections.

### 7.2.3 Scope and limitations of the current simulations

It is important to emphasize that the present simulations represent a baseline design rather than an optimized device. The waveguide geometry is fixed throughout the switching region, and no adiabatic or mode-engineered transitions are employed. As a result, the reported insertion loss should be interpreted as a conservative estimate.

In practical integrated photonic designs, several well-established techniques can significantly reduce loss:

- Gradual narrowing or widening of the waveguide in coupling regions to improve mode matching,

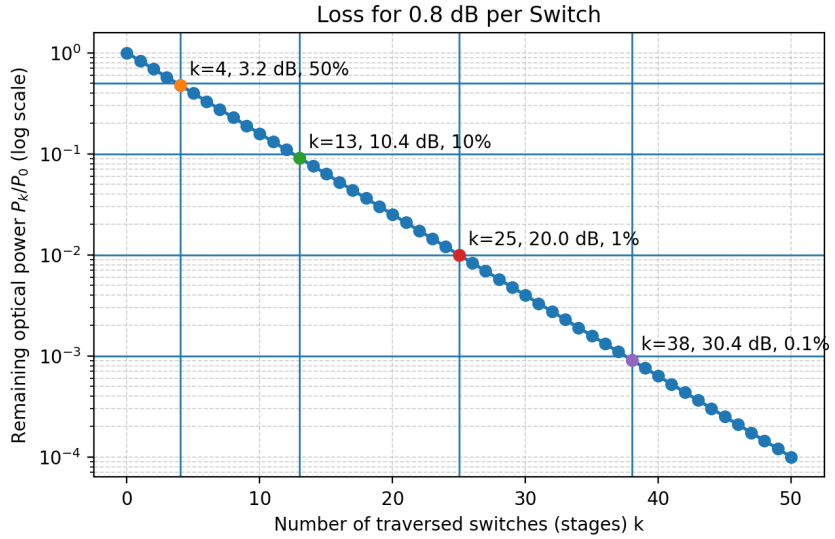


Figure 7.2: Accumulated insertion loss for vertically cascaded switching stages assuming a single-switch insertion loss of 0.8 dB.

Horizontal lines indicate common power thresholds (3 dB, 10 dB, 20 dB, and 30 dB), illustrating practical limits on the number of cascaded switches.

- The use of optimized s-bend geometries based on clothoid or Euler curves to suppress radiation loss [18],
- Local waveguide width modulation inside multimode or interferometric regions to enhance self-imaging fidelity,
- Transition tapers between straight and curved sections to reduce scattering and reflection.

These techniques are not included in the present simulations, but are expected to substantially improve transmission efficiency when incorporated into a refined design.

#### 7.2.4 Interpretation and outlook

Taken together, the preliminary results indicate that while the current implementation exhibits non-negligible insertion loss, its qualitative switching behavior is robust, with low crosstalk and stable routing in the CROSS state. The observed loss levels primarily reflect the absence of geometric and modal optimization rather than fundamental architectural limitations.

Consequently, the results presented here should be viewed as establishing a conservative lower bound on achievable performance. Future work will focus on incorporating device-level optimization techniques and completing BAR-state characterization, enabling a more comprehensive evaluation of switching performance and scalability under realistic fabrication constraints.

### 7.3 Comparison of Switch Element Sizes

The choice of the fundamental switch element plays a critical role in determining the overall performance, scalability, and physical feasibility of an optical switching network. In this section,  $2 \times 2$ ,  $3 \times 3$ , and general  $M \times M$  switch elements are compared in terms of network depth, hardware complexity, and suitability for integrated photonic implementations.

**$2 \times 2$  switch elements** Switching networks composed of  $2 \times 2$  elements represent the most commonly studied and experimentally demonstrated case in integrated photonics. These switches are typically implemented using Mach–Zehnder interferometers or directional couplers and benefit from mature fabrication processes and well-understood calibration procedures. From an architectural perspective,  $2 \times 2$  switches offer maximal routing flexibility and simple local control. However, achieving non-blocking operation for large  $N$  requires a relatively large number of stages, leading to a network depth that scales linearly with  $N$ . As a result, accumulated insertion loss and phase errors can become a limiting factor for large-scale systems.

**$3 \times 3$  switch elements** Increasing the switch size to  $3 \times 3$  allows multiple channels to be routed simultaneously, reducing the required number of switching stages for a given network size. Compared to  $2 \times 2$  architectures, this reduction in depth can significantly lower the worst-case optical loss and improve overall signal fidelity. However,  $3 \times 3$  switches introduce additional internal complexity, including more interferometric paths and a larger number of phase shifters. This increases sensitivity to fabrication imperfections and calibration errors. Consequently, while  $3 \times 3$  switches offer improved architectural efficiency, they demand more sophisticated control and stabilization techniques.

**General  $M \times M$  switch elements** Extending this concept to general  $M \times M$  switch elements further amplifies the architectural benefits. Larger switches enable a proportional reduction in network depth, and can substantially reduce the total number of switch layers required. This property is particularly attractive for quantum photonic networks, where minimizing optical loss is essential. At the same time, the internal structure of an  $M \times M$  switch grows rapidly in complexity as  $M$  increases, resulting in a larger footprint, higher control overhead, and increased susceptibility to phase noise and thermal crosstalk. These factors impose practical upper limits on feasible switch sizes in integrated platforms.

**Architectural trade-offs** The comparison highlights a fundamental trade-off between network-level efficiency and component-level complexity. Smaller switch elements offer robustness and simplicity but lead to deeper networks, while larger switch elements reduce depth at the expense of increased internal complexity and calibration effort. The proposed switching architecture accommodates this trade-off by allowing the switch size  $M$  to be selected according to system requirements and fabrication constraints. In practice, intermediate switch sizes, such as  $3 \times 3$  or  $4 \times 4$ , may offer a favorable balance between depth reduction and implementation complexity.

Table 7.1: Representative MMI-based optical switches with explicitly reported insertion loss in telecom wavelengths.

Paper	Switch size	Platform	Reported loss
Rosa et al. [2]	$2 \times 2$	SOI (silicon photonics)	$\sim 0.5$ dB
Truong et al. [1]	$3 \times 3$	Dielectric / $\text{SiO}_2$	$\sim 0.65$ dB
Thanh [40]	$4 \times 4$	SOI (CMOS-compatible)	$\sim 0.46$ dB

In summary, while  $2 \times 2$  switches remain attractive for their simplicity and maturity, larger  $M \times M$  switch elements provide a promising path toward scalable, low-depth optical switching networks. The flexibility of the proposed design enables adaptation to different switch sizes, making it suitable for a wide range of quantum photonic applications.

## 7.4 Literature-Based Loss Analysis and Discussion

Electromagnetic simulations of the proposed switching elements indicate that basic implementations of directional coupler and MZI-based switches can exhibit relatively large insertion losses, which may limit scalability when extrapolated to large network sizes. Rather than interpreting this as a limitation of the switching architecture itself, this result motivates a comparison with optimized switch implementations reported in the literature.

In particular, apart from MZI based switches, multimode interference (MMI)-based switches have been widely demonstrated as low-loss and fabrication-tolerant alternatives for integrated photonic switching. Since the present work targets architectural scalability rather than device-level optimization, representative per-switch loss values reported in the literature are used to evaluate chip-level loss trends.

It should be noted that most low-loss MMI switches reported to date operate at telecom wavelengths, where fabrication processes and material platforms are highly optimized. In contrast, integrated switching at visible wavelengths, including 422 nm, remains comparatively underexplored, and higher loss is therefore expected. The simulation results presented in this work should thus be regarded as baseline estimates, highlighting the importance of continued device-level optimization for visible-wavelength operation.

Table 7.1 and Fig. 7.3 together illustrate that the lowest-loss switching architecture is not determined solely by the switch size. While  $2 \times 2$  switches are often assumed to provide the lowest insertion loss, the figure shows that, for the selected implementations, the  $4 \times 4$  switch yields the lowest aggregate chip-level loss over a wide range of network sizes. This outcome reflects the combined effect of per-switch loss and total switch count, rather than either factor alone. Since there are no papers on larger size switches within visible wavelength, this table and figure only include switches operating at telecom wavelengths.

These results emphasize that optimal switch size depends strongly on the underlying technology platform and fabrication maturity. Consequently, architectural design should be informed by the availability and performance of practical switch implementations, rather than assuming that smaller switch elements always lead to lower loss. Evaluating candidate switch technologies in conjunction with network-level scaling therefore provides a more realistic basis for selecting the most suitable switch size for large-scale photonic

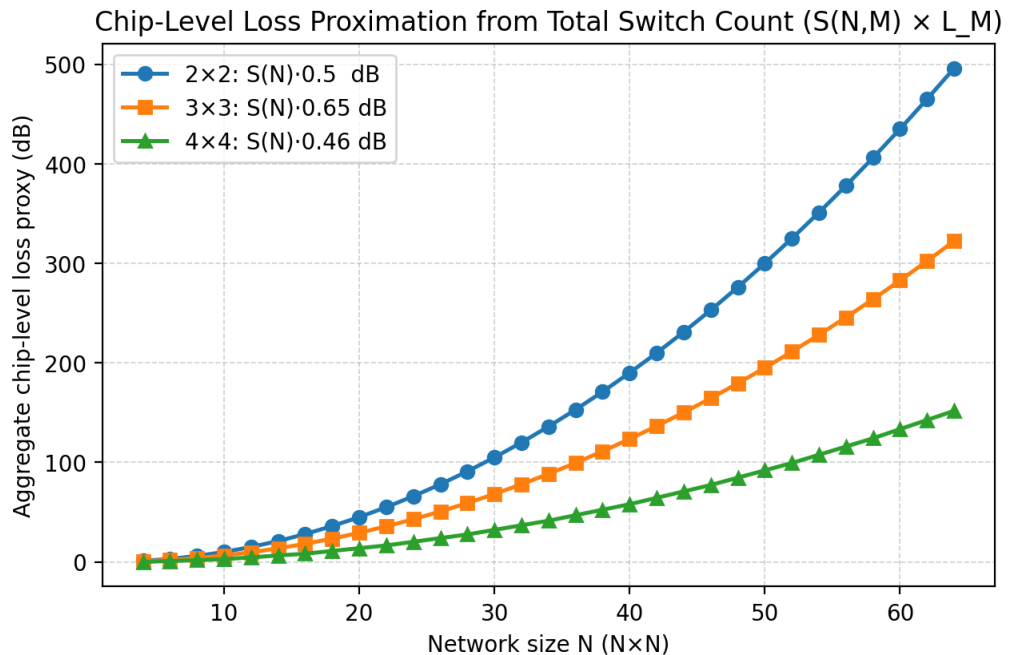


Figure 7.3: Estimated chip-level loss proxy based on literature-reported switch losses. The plot estimates the total insertion loss for an  $N \times N$  switching network constructed from  $2 \times 2$ ,  $3 \times 3$ , and  $4 \times 4$  MMI-based switches, using representative per-switch loss values from the literature. The results highlight the trade-off between switch size, total switch count, and aggregate loss.

switching fabrics.

# Chapter 8

## Conclusion

This thesis investigated the design and evaluation of scalable optical switching networks for quantum photonic applications, with emphasis on architectural efficiency and physical realizability on integrated photonic platforms. Motivated by the strict loss and scalability requirements of quantum networks, a recursive switching architecture based on  $M \times M$  switch elements was proposed and analyzed.

At the architectural level, the proposed design exploits a deterministic recursive reduction strategy to construct non-blocking  $N \times N$  switching networks with favorable scaling properties. Compared to naive crossbar approaches, the total number of switch elements scales subquadratically.

At the device level, electromagnetic simulations were performed to characterize the basic switching behavior of an individual element in both the CROSS and BAR states. The results confirm correct routing functionality with low crosstalk in both operating states, while highlighting non-negligible insertion loss in the present baseline design. The BAR state exhibits slightly higher insertion loss than the CROSS state, consistent with the scattering-matrix analysis presented in earlier chapters, but maintains acceptable isolation between output ports. Importantly, the observed losses are attributed primarily to the absence of geometric and modal optimization, rather than to inherent limitations of the proposed architecture. A literature-based comparison further supports this interpretation, showing that optimized MMI-based switches can achieve significantly lower per-element loss, and that larger switch elements may offer lower aggregate chip-level loss when network-scale effects are considered.

Taken together, these results demonstrate that the proposed switching architecture provides a scalable and physically motivated framework for large-scale quantum photonic networks. By jointly considering architectural structure and device-level performance, this work establishes a foundation for systematic exploration of low-loss, high-connectivity optical switching fabrics suitable for quantum information processing.

### 8.1 Future Work

While this thesis establishes the feasibility and advantages of the proposed switching architecture, several important directions remain for future investigation.

### 8.1.1 Extension to Multicomputer Network Architectures

From a network-architecture perspective, the present work focuses primarily on a single large switching fabric. An important extension is the development of switching designs tailored for *modular quantum computing* architectures, where multiple quantum processors are interconnected via optical links. In such systems, the switching network must support not only full connectivity, but also efficient routing between distinct computational modules, shared entanglement-generation resources, and hierarchical or heterogeneous network topologies.

Future work will explore how proposed recursive switching principles can be adapted to multi-level architectures, such as hierarchical, tree-based, and cluster-oriented interconnects.

### 8.1.2 Device-Level Optimization and Fabrication-Oriented Design

At the device level, the current simulations represent a conservative baseline implementation. Next step is to pursue a fully optimized chip design that minimizes insertion loss and improves robustness against fabrication imperfections. This includes incorporating adiabatic transitions, optimized S-bend geometries, mode-engineered coupling regions, and waveguide tapers, as well as refining interferometric layouts to improve phase stability and extinction ratio.

Ultimately, these efforts aim to bridge simulation and experimental realization, paving the way toward fabricated low-loss photonic switches operating at visible wavelengths.

### 8.1.3 Outlook

By combining scalable architectural design with physically grounded device evaluation, this thesis contributes toward the development of practical optical switching networks for quantum technologies. Continued progress along both architectural and device-level directions will be essential for realizing large-scale, low-loss quantum photonic interconnects capable of supporting future quantum communication and distributed quantum computing systems.

# Acknowledgment

I would like to express my sincere gratitude to all those who supported and guided me throughout my undergraduate research.

I would like to thank Professor Rodney Van Meter for introducing me to the field of quantum information and switching networks. The guidance and insight strongly influenced my academic direction, and the opportunities provided allowed me to explore this field deeply and develop a strong interest in quantum networking and photonic systems.

I would also like to express my sincere appreciation to Associate Professor Shota Nagayama for his continuous support, technical guidance, and encouragement throughout this project. I am particularly grateful for the opportunities he provided, which broadened my perspective and strengthened my motivation for research. I am also grateful to Associate Professor Michal Hajdušek for his valuable advice and discussions. His insights, especially regarding optics and physical intuition behind photonic systems, played an important role in shaping this work.

I would like to thank Hikaru Yokomori for his consistent guidance and support across this and other research activities. I also extend my sincere thanks to Assistant Professor Amin Taherkhani and Assistant Professor Naphan Benchasattabuse for their helpful feedback and support.

My sincere thanks go to the members of the Optical Switch Unit, Junseo Kwak and Manasvi Patwardhan, as well as the graduate students in the group, for their advice on thesis writing.

I also acknowledge the support of the JST Moonshot R&D Program under Grant Numbers JPMJMS226C and JPMJMS2061. I would further like to thank the AQUA members, whose encouragement and friendly atmosphere made both research and daily life enjoyable.

I am deeply grateful to Associate Professor David Elkouss for welcoming me to his unit at OIST during my research internship and for providing me with the opportunity to deepen my understanding of quantum information and quantum networks. I also thank the members of his unit for the enriching time at OIST, and in particular Joshua Casapao for his guidance and advice on my research project.

Finally, I would like to thank my parents for their constant support and for allowing me to pursue what I enjoy. I also thank my sister for her continued encouragement.

I am also deeply grateful to my friends, affectionately known as “zesty.” Many of my best memories were made with them, and their humor and perspective made even the busiest days enjoyable. The vibes were always on point.

# Bibliography

- [1] 3×3 multimode interference optical switches using electro-optic effects as phase shifters. *Optics Communications*, Vol. 292, pp. 78–83, 2013.
- [2] Álvaro Rosa, Ana Gutiérrez, Antoine Brumont, Amadeu Griol, and Pablo Sanchis. High performance silicon 2x2 optical switch based on a thermo-optically tunable multimode interference coupler and efficient electrodes. *Opt. Express*, Vol. 24, No. 1, pp. 191–198, Jan 2016.
- [3] Ansys. Fde solver analysis - mode list and deck. <https://optics.ansys.com/hc/en-us/articles/360034396734-FDE-solver-analysis-Mode-List-and-Deck> (accessed: 2025-12-19).
- [4] Ansys. Heat solver introduction. <https://optics.ansys.com/hc/en-us/articles/360034917713-HEAT-solver-introduction> (accessed: 2025-12-19).
- [5] Ansys. Mode - eigenmode expansion (eme) solver introduction. <https://optics.ansys.com/hc/en-us/articles/360034396614-MODE-EigenMode-Expansion-EME-solver-introduction> (accessed: 2025-12-19).
- [6] Charles H. Bennett and Gilles Brassard. Quantum cryptography: Public key distribution and coin tossing. *Theoretical Computer Science*, Vol. 560, pp. 7–11, 2014. Theoretical Aspects of Quantum Cryptography – celebrating 30 years of BB84.
- [7] Charles H. Bennett, Gilles Brassard, Claude Crépeau, Richard Jozsa, Asher Peres, and William K. Wootters. Teleporting an unknown quantum state via dual classical and einstein-podolsky-rosen channels. *Phys. Rev. Lett.*, Vol. 70, No. 13, pp. 1895–1899, 1993.
- [8] H.-J. Briegel, W. Dür, J. I. Cirac, and P. Zoller. Quantum repeaters: The role of imperfect local operations in quantum communication. *Phys. Rev. Lett.*, Vol. 81, pp. 5932–5935, 1998.
- [9] Marcello Caleffi, Michele Moretti, Davide Ferrari, Daniele Cuomo, Jessica Illiano, Antonio Manzalini, and Angela Sara Cacciapuoti. Distributed quantum computing: A survey. *Comput. Net.*, Vol. 254, p. 110672, 2024.
- [10] Nitesh et al. Chauhan. Ultra-low loss visible light waveguides for integrated atomic, molecular, and quantum photonics. *Optics Express*, Vol. 30, pp. 6960–6969, 2022.

- [11] X. Chen, Jiao Lin, and Ke Wang. A review of silicon-based integrated optical switches. *Laser & Photonics Reviews*, 2023.
- [12] J. I. Cirac, A. K. Ekert, S. F. Huelga, and C. Macchiavello. Distributed quantum computation over noisy channels. *Phys. Rev. A*, Vol. 59, pp. 4249–4254, Jun 1999.
- [13] Robert J. Drost, Terrence J. Moore, and Michael Brodsky. Switching networks for pairwise-entanglement distribution. *Journal of Optical Communications and Networking*, Vol. 8, No. 5, pp. 331–342, 2016.
- [14] Pierre Dubé, Alan A. Madej, Zichao Zhou, and John E. Bernard. Evaluation of systematic shifts of the  $^{88}\text{Sr}^+$  single-ion optical frequency standard at the  $10^{-17}$  level. *Physical Review A*, Vol. 87, No. 2, p. 023806, 2013.
- [15] Pierre Dubé, Allan Shiner, Bijun Jian, Alan A. Madej, and John E. Bernard.  $^{88}\text{Sr}^+$  single-ion optical clock with a stability approaching the quantum projection noise limit. *Physical Review A*, Vol. 92, No. 4, p. 042119, 2015.
- [16] Artur K. Ekert. Quantum cryptography based on bell’ s theorem. *Phys. Rev. Lett.*, Vol. 67, No. 6, pp. 661–663, 1991.
- [17] Fulvio Flamini, Nicolò Spagnolo, and Fabio Sciarrino. Photonic quantum information processing: a review. *Reports on Progress in Physics*, Vol. 82, p. 016001, 2018.
- [18] Takeshi Fujisawa, Shuntaro Makino, Takanori Sato, and Kunimasa Saitoh. Low-loss, compact, and fabrication-tolerant si-wire 90° waveguide bend using clothoid and normal curves for large scale photonic integrated circuits. *Opt. Express*, Vol. 25, No. 8, pp. 9150–9159, Apr 2017.
- [19] Scarlett Gauthier, Gayane Vardoyan, and Stephanie Wehner. A control architecture for entanglement generation switches in quantum networks. In *Proceedings of the 1st Workshop on Quantum Networks and Distributed Quantum Computing*, New York, NY, USA, 2023. Association for Computing Machinery.
- [20] Vittorio Giovannetti, Seth Lloyd, and Lorenzo Maccone. Quantum metrology. *Phys. Rev. Lett.*, Vol. 96, p. 010401, Jan 2006.
- [21] Nicolas Gisin, Grégoire Ribordy, Wolfgang Tittel, and Hugo Zbinden. Quantum cryptography. *Rev. Mod. Phys.*, Vol. 74, pp. 145–195, 2002.
- [22] Michal Hajdušek and Rodney Van Meter. *Quantum Communications*. 2023.
- [23] Richard Jozsa, Daniel S. Abrams, Jonathan P. Dowling, and Colin P. Williams. Quantum clock synchronization based on shared prior entanglement. *Phys. Rev. Lett.*, Vol. 85, pp. 2010–2013, Aug 2000.
- [24] H. Jeff Kimble. The quantum internet. *Nature*, Vol. 453, pp. 1023–1030, 2008.
- [25] Marii Koyama, Claire Yun, Amin Taherkhani, Naphan Benchasattabuse, Bernard Ousmane Sane, Michal Hajdušek, Shota Nagayama, and Rodney Van Meter. Optimal Switching Networks for Paired-Egress Bell State Analyzer Pools. In *2024 International Conference on Quantum Computing and Engineering*, 5 2024.

- [26] A. Kramida, Yu. Ralchenko, J. Reader, and NIST ASD Team. Nist atomic spectra database (ver. 5.12). <https://physics.nist.gov/asd>, 2024. National Institute of Standards and Technology, Gaithersburg, MD. Accessed: 2025-12-23.
- [27] Feng-Yu Lu, Ze-Hao Wang, Yao Zhou, Yu-Xuan Fan, et al. Fully heterogeneous prepare-and-measure quantum network for the next stage of quantum internet. *Nature Communications*, 2025.
- [28] C. Monroe, et al. Large-scale modular quantum-computer architecture with atomic memory and photonic interconnects. *Physical Review A*, Vol. 89, p. 022317, 2014.
- [29] Michael A. Nielsen and Isaac L. Chuang. *Quantum Computation and Quantum Information: 10th Anniversary Edition*. Cambridge University Press, 2010.
- [30] Tracy E. Northup and Rainer Blatt. Quantum information transfer using photons. *Nature Photonics*, Vol. 8, pp. 356–363, 2014.
- [31] Jeremy L. O’Brien, Akira Furusawa, and Jelena Vučković. Photonic quantum technologies. *Nature Photonics*, Vol. 3, pp. 687–695, 2009.
- [32] Gaspar Mendes Rego. Temperature dependence of the thermo-optic coefficient of geo2-doped silica glass fiber. *Sensors*, Vol. 24, No. 15, 2024.
- [33] Daisuke Sakuma, Amin Taherkhani, Tomoki Tsuno, Toshihiko Sasaki, Hikaru Shimizu, Kentaro Teramoto, Andrew Todd, Yosuke Ueno, Michal Hajdusek, Rikizo Ikuta, Rodney Meter, and Shota Nagayama. An optical interconnect for modular quantum computers. 12 2024.
- [34] Bahaa E.A. Saleh and Malvin Carl Teich. *Fundamentals of Photonics*. John Wiley & Sons, 3 edition, 2019.
- [35] J. E. Sansonetti. Wavelengths, transition probabilities, and energy levels for the spectra of strontium ions (Sr II through Sr XXXVIII). *Journal of Physical and Chemical Reference Data*, Vol. 41, No. 1, p. 013102, 2012.
- [36] Hassan Shapourian, Eneet Kaur, Troy Sewell, Jiapeng Zhao, Michael Kilzer, Ramana Kompella, and Reza Nejabati. Quantum data center infrastructures: A scalable architectural design perspective. 01 2025.
- [37] Stephanie Simmons. Scalable fault-tolerant quantum technologies with silicon color centers. *PRX Quantum*, Vol. 5, p. 010102, Mar 2024.
- [38] R. A. Spanke and V. E. Benes. N-stage planar optical permutation network. *Appl. Opt.*, Vol. 26, No. 7, pp. 1226–1229, Apr 1987.
- [39] L. J. et al. Stephenson. High-rate, high-fidelity entanglement of qubits across an elementary quantum network. *Phys. Rev. Lett.*, Vol. 124, p. 110501, 2020.
- [40] Le Trung Thanh. Arbitrary power splitting couplers based on 4x4 multimode interference structures for vlsi photonic integrated circuits. New York, NY, USA, 2011. Association for Computing Machinery.

- [41] Rodney Van Meter. *Quantum Networking*. Wiley, 2014.
- [42] Jianwei Wang, Fabio Sciarrino, Anthony Laing, and Mark G. Thompson. Integrated photonic quantum technologies. *Nature Photonics*, Vol. 14, pp. 273–284, 2020.
- [43] Stephanie Wehner, David Elkouss, and Ronald Hanson. Quantum internet: A vision for the road ahead. *Science*, Vol. 362, No. 6412, p. eaam9288, 2018.
- [44] Zhaoming Zhu and Thomas G. Brown. Full-vectorial finite-difference analysis of microstructured optical fibers. *Optics Express*, Vol. 10, No. 17, pp. 853–864, 2002.
- [45] Marek Żukowski, Anton Zeilinger, Michael A. Horne, and Artur K. Ekert. “event-ready-detectors” bell experiment via entanglement swapping. *Physical Review Letters*, Vol. 71, pp. 4287–4290, 1993.